

AD-A239 733

2

PL-TR-91-2069



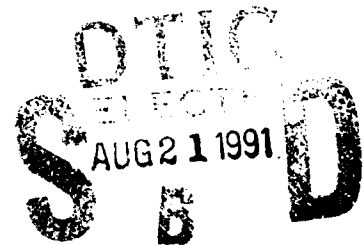
**IMAGING THE MORPHOTECTONIC SETTING OF SEISMIC EVENTS
AND THEIR PROPAGATION PATHS: METHODOLOGY AND
COMPARATIVE STUDIES**

Bryan L. Isacks
Muawia Barazangi
Eric J. Fielding
Richard W. Allmendinger

Cornell University
Institute for the Study of
the Continents
Snee Hall
Ithaca, NY 14853-1504

20 March 1991

Final Technical Report
20 July 1988-20 January 1991



APPROVED FOR PUBLIC RELEASE; DISTRIBUTION UNLIMITED



PHILLIPS LABORATORY
AIR FORCE SYSTEMS COMMAND
HANSCOM AIR FORCE BASE, MASSACHUSETTS 01731-5000

91 8 20 833

91-08327



SPONSORED BY
Defense Advanced Research Projects Agency
Nuclear Monitoring Research Office
ARPA ORDER NO. 5299

MONITORED BY
Phillips Laboratory
Contract F19628-88-K-0035

The views and conclusions contained in this document are those of the authors and should not be interpreted as representing the official policies, either expressed or implied, of the Defense Advanced Research Projects Agency or the U.S. Government.

This technical report has been reviewed and is approved for publication.



JAMES F. LEWKOWICZ
Contract Manager
Solid Earth Geophysics Branch
Earth Sciences Division



JAMES F. LEWKOWICZ
Branch Chief
Solid Earth Geophysics Branch
Earth Sciences Division



DONALD H. ECKHARDT, Director
Earth Sciences Division

This report has been reviewed by the ESD Public Affairs Office (PA) and is releasable to the National Technical Information Service (NTIS).

Qualified requestors may obtain additional copies from the Defense Technical Information Center. All others should apply to the National Technical Information Service.

If your address has changed, or if you wish to be removed from the mailing list, or if the addressee is no longer employed by your organization, please notify PL/IMA, Hanscom AFB, MA 01731-5000. This will assist us in maintaining a current mailing list.

Do not return copies of this report unless contractual obligations or notices on a specific document requires that it be returned.

REPORT DOCUMENTATION PAGE			Form Approved OMB No. 0704-0188	
Public reporting burden for this collection of information is estimated to average 1 hour per response, including the time for reviewing instructions, searching existing data sources, gathering and maintaining the data needed, and completing and reviewing the collection of information. Send comments regarding this burden estimate or any other aspect of this collection of information, including suggestions for reducing this burden, to Washington Headquarters Services, Directorate for Information Operations and Reports, 1215 Jefferson Davis Highway, Suite 1204, Arlington, VA 22202-4302, and to the Office of Management and Budget, Paperwork Reduction Project (0704-0188), Washington, DC 20503				
1. AGENCY USE ONLY (Leave blank)		2. REPORT DATE 20 March 1991	3. REPORT TYPE AND DATES COVERED Final (20 July 1988-20 January 1991)	
4. TITLE AND SUBTITLE Imaging the Morphotectonic Setting of Seismic Events and Their Propagation Paths: Methodology and Comparative Studies			5. FUNDING NUMBERS PE 62714E PR 8A10 TA DA WU AN Contract F19628-88-K-0035	
6. AUTHOR(S) Bryan L. Isacks Muawia Barazangi Richard W. Allmendinger				
7. PERFORMING ORGANIZATION NAME(S) AND ADDRESS(ES) Cornell University Institute for the Study of the Continents, Snee Hall Ithaca, NY 14853-1504			8. PERFORMING ORGANIZATION REPORT NUMBER	
9. SPONSORING/MONITORING AGENCY NAME(S) AND ADDRESS(ES) Phillips Laboratory Hanscom AFB, MA 01731-5000 Contract Manager: James Lewkowicz/LWH			10. SPONSORING/MONITORING AGENCY REPORT NUMBER PL-TR-91-2069	
11. SUPPLEMENTARY NOTES				
12a. DISTRIBUTION/AVAILABILITY STATEMENT Approved for public release; Distribution unlimited			12b. DISTRIBUTION CODE	
13. ABSTRACT (Maximum 200 words) <p>Geomorphic interpretation of geologic features using DEMs (Digital Elevation Models) and satellite imagery can yield useful information on long-term fault activity in the absence of detailed ground mapping. Mapping of probable active faults in Central Asia and estimation of the type of offset from DEMs is combined with digitizations of published fault maps, Landsat TM and SPOT imagery, and earthquake catalogs in a Geographic Information System to provide information on the probability that a shallow seismic event is a natural earthquake, thus aiding in the verification of nuclear test ban treaties. Topographic characteristics are analyzed at resolutions from 100 m to 50 km.</p> <p>Several studies have noted the lack of propagation of high-frequency L_g waves across major mountain ranges, such as the Himalaya-Pamirs and Sierra Nevada. Extreme surface roughness caused by fluvial and glacial erosion may significantly contribute to explaining the lack of propagation across high mountain ranges. Use of L_g amplitudes along such paths for discrimination or yield estimation could be invalid or require correction factors. Profiles of topography in a swath along the propagation path of L_g from a given event show the amount of topographic relief at the surface that could contribute to scattering high-frequency energy.</p>				
14. SUBJECT TERMS Digital Elevation Models, satellite imagery, Geographic Information Systems, L_g propagation, surface roughness, topographic relief			15. NUMBER OF PAGES 84	
			16. PRICE CODE	
17. SECURITY CLASSIFICATION OF REPORT Unclassified	18. SECURITY CLASSIFICATION OF THIS PAGE Unclassified	19. SECURITY CLASSIFICATION OF ABSTRACT Unclassified	20. LIMITATION OF ABSTRACT SAR	

TABLE OF CONTENTS

Abstract	i
List of Figures	iv
List of Tables	v
Bibliography of Publications Sponsored by the Contract	v
Summary	vi
Introduction	1
Objectives	2
Results	3
Topography	4
Processing	9
Visualization tools	10
Analysis	17
Data Limitations: Gaps, Artifacts, and Resolution	25
Geological and Geophysical Data	33
Technique Development	33
Digital Map Datasets	37
Satellite Imagery	44
SPOT	44
Other	50
Comparisons	53
Data Products	57
Products Generated	57
Plans to Transfer Products to CSS	58
Conclusions and Recommendations	59
References	61



Accession For	
NTIS GRA&I	<input checked="" type="checkbox"/>
DTIC TAB	<input type="checkbox"/>
Unannounced	<input type="checkbox"/>
Justification	
By	
Distribution/	
Availability Codes	
Dist	Avail and/or Special
A-1	

LIST OF FIGURES

Figure 1. Map of Eurasia showing area covered by mosaics of digital topography	5
Figure 2. Overview map of Central Asia showing coverage of DTED cells received.	6
Figure 3. Grey-scale mosaic of Central Asia DTED cells processed.	11
Figure 4. Shaded relief rendering of Lambert projection 5 km resolution mosaic for Central Asia.	14
Figure 5. Synthetic 3D perspective view looking from south to the north showing a system of faults to the east of Tibet in the Nan Shan of central China.	17
Figure 6. Synthetic 3D perspective view like that of Figure 5, showing part of the active normal fault system near Lake Baikal.	19
Figure 7. Gray-scale mosaic of surface roughness calculated from the Central Asia DTED.	20
Figure 8. Map showing locations of Lg propagation paths for which the topographic profiles are shown in Figure 9.	23
Figure 9. Topographic profiles along swaths centered on great circle paths of Lg propagation	24
Figure 10. Grey-scale two dimensional Fourier power spectrum of a 512x512 pixel portion of the DTED near latitude 55°N and longitude 110°E.	28
Figure 11. Map of DTED cells covering the southwest part of Novaya Zemlya.	30
Figure 12. Gray-scale mosaic of DTED cells covering the southwest part of Novaya Zemlya.	32
Figure 13. Map showing a detail of one degree square (32–33°N, 90–91°E) of the digitized geology coverage of the Geotraverse across Tibet	34
Figure 14. Small-scale overview map of published Late Cenozoic faults in Central Asia, digitized and integrated into ARC/INFO.	39
Figure 15. Map showing location of the digitized geology coverage of the Geotraverse across Tibet.....	40
Figure 16. Map showing the digitized geology coverage of the southern half of Geotraverse across Tibet.....	41
Figure 17. Map of annual precipitation and topography for Central Asia.....	43
Figure 18. Map showing coverage of SPOT scenes acquired for Central Asia... ..	45
Figure 19. SPOT image of area around Nanga Parbat, Pakistan.	48
Figure 20. Map of the area around the Kazakhstan test site in the Soviet Union, showing seismic events, known explosions, and coverage of Landsat TM image	52

LIST OF TABLES

Table 1. Cornell Asia Topography Acquired	8
Table 2. Cornell Asia Topography List of Missing Cells for Data Acquired	26
Table 3. Cornell SPOT Central Asia Imagery Acquired	45
Table 4. Cornell Satellite Imagery 1990 Outstanding	47
Table 5. Cornell SPOT Imagery for South America Acquired	50
Table 6. Comparison of Locations Determined from SPOT and GPS	56

BIBLIOGRAPHY OF PUBLICATIONS SPONSORED BY THE CONTRACT

Abstracts

Fielding, E.J., T.L. Gubbels, and B.L. Isacks, 1989, "Optimal Digital Elevation Model Resolution for the Interpretation of Morphotectonics", in *EOS Transactions of the American Geophysical Union, Vol 70, No 15*, April 11, 1989, pg. 467.

Fielding, E.J., Isacks, B.L., and Gubbels, T.L., 1989, Regional neotectonic analysis in the Central Andes and Central Asia using a morphotectonic information system, *GSA Abstr. with Prog.*, v. 21, no. 6, p. A178-179.

Fielding, E J, B L Isacks, and M Barazangi, 1990, Tectonic Expression of Active Faults in Central Asia: Methodology and Implications for Nuclear Test Ban Treaties, *EOS, Trans. AGU*, v. 71, no. 17, p. 560.

Papers

Fielding, E.J., T.L. Gubbels, and B.L. Isacks, 1989, "Optimal Digital Elevation Model Resolution for the Interpretation of Morphotectonics", in *Papers presented at 11th Annual DARPA/AFGL Seismic Research Symposium*, p. 221-230.

Fielding, Eric J., Bryan L. Isacks, and Muawia Barazangi, 1990, "Topographic Expression of Active Faults in Central Asia and Topographic Relief Effects on L_g Propagation", in *Papers Presented at 12th Annual DARPA/GL Seismic Research Symposium*, p. 257-263.

SUMMARY

Geomorphic interpretation of geologic features using DEMs (Digital Elevation Models) and satellite imagery can yield useful information on long-term fault activity in the absence of detailed ground mapping. Mapping of probable active faults in Central Asia and estimation of the type of offset from DEMs is combined with digitizations of published fault maps, Landsat Thematic Mapper and SPOT imagery where available, and earthquake catalogs in a Geographic Information System to provide information on the probability that a shallow seismic event is a natural earthquake, thus aiding in the verification of nuclear test ban treaties. Topographic characteristics of active fault zones are analyzed on DEMs at a range of resolutions from 100 m to 10 km. A Central Asia mosaic of relatively crudely sampled topography (~1 km grid) clearly shows the large uplifted mountain blocks and major active fault zones, such as the Altyn Tagh, Karakoram, and Lake Baikal fault zones. We used medium-resolution DEMs (~100 m grid) to delineate individual fault scarps and tilted strata on the limbs of folds and fault blocks. Geomorphic features diagnostic of youthful activity, such as pressure ridges, offsets in river channels, scarps in alluvial fans, and tilted or uplifted geomorphic surfaces are visible on the full resolution data with shaded-relief synthetic stereo and perspective rendering. Estimation of the amount and age of fault activity depends on many factors, especially the geologic unit involved, the rate of erosion in the area (which depends on climate), and the type of the fault. Normal and strike-slip faults generally have clearer topographic expressions than thrust faults.

Several studies have noted the lack of propagation of high-frequency L_g waves across major mountain ranges, such as the Central Andes, Himalaya-

Pamirs, and Sierra Nevada. Extreme surface roughness caused by fluvial and glacial erosion may significantly contribute to explaining the lack of propagation across high mountain ranges. Use of L_g amplitudes along such paths for discrimination or yield estimation could be invalid or require correction factors. Surface roughness is calculated from the DEMs by finding the topographic relief (maximum minus minimum elevation) within a series of different-sized moving windows ranging from $\sim 2 \times 2$ km to $\sim 60 \times 60$ km. Topographic relief in Central Asia, measured this way, varies greatly from flat alluvial basins (relief near zero) to dissected high mountains (relief > 1000 m within 2–10 km wavelengths). The Tien Shan has moderately high relief of more than 500 m for most of its length and width. The Himalayan front along the southern edge of the Tibetan Plateau and much of the northern edge both have high to very high relief (1000–2500 m over a 2 km wavelength) surrounding the plateau, with wider zones of high relief at the western end, the Pamirs and Hindu Kush, and at the eastern end in south-central China. Profiles of topography in a swath along the propagation path of L_g from a given event show the amount of topographic relief at the surface that could contribute to scattering high-frequency energy.

The methodology that we have developed under this contract for processing and analyzing digital topography, satellite imagery, and map datasets has matured into an effective system. We are in the process of making both the datasets generated and the methodology used to generate them available to DARPA through the CSS. We describe in this report the methodology for the analysis of these processed datasets.

INTRODUCTION

Successful monitoring of a comprehensive or threshold nuclear test ban treaty depends on the integration of many different types of data. Seismic data have been central to the problem, but the trail of seismic research has now reached the point where traditional "layer cake" structures need to be replaced by models with more geologically realistic heterogeneous structure and topography. For example, it is likely that the excitation, propagation and reception of the L_g phase at regional and continental scale distances is strongly controlled by surface topography, sedimentary basins, changes in crustal thickness and structure as well as by the nature of the source itself. Yield estimation is critically dependent upon these geological complexities. The important controlling features are specific to the particular locations of the sources, stations and propagation paths. They can be determined only by amalgamation of diverse datasets on topography, potential fields, seismicity, tectonics, crustal structure and geology. The basic premise of this project is that the increasing sophistication in analysis of seismic waves must be matched by advances in the ability to capture and apply available geophysical, geological, and topographical data relevant to the propagation of seismic waves along specific regional or continental scale paths.

The prototype Intelligent Monitoring System (IMS) now running at the Center for Seismic Studies (CSS) includes interlocking modules that do automated seismic signal analysis for the detection and identification of events and their phases, that allow interactive analysis and manipulation of digital seismograms, that estimate magnitude of events and the yield of explosions, that search various catalogs for events with certain characteristics, and that present the results of event locations on a relatively simple map background. The

present version of the IMS has few provisions for utilizing geological and geophysical information to analyze the event location, and has no provisions for examining these types of data for the propagation paths.

The aim of this project was to design a methodology for collecting and organizing available geological and geophysical datasets such as satellite imagery, digital topography, geologic maps for Central Asia into a geographic information system (GIS) that can be incorporated into future versions of the IMS to aid in the quantification of region-specific source and propagation characteristics. We also developed visualization and analysis techniques for utilizing the three-dimensional data from our GIS that can be incorporated into routine and research analyses at the CSS.

The choice of data, its capture and ingestion, and the methods for integration into a monitoring system all require experience in regional-scale continental tectonics and crustal structure. Effective utilization of voluminous satellite, topographical, geological and geophysical datasets is one of the major scientific challenges of the future, one that will have enormous impacts on earth science in general as well as on specific applications such nuclear test detection and verification.

OBJECTIVES

The project had two related objectives. The first was to develop an integrated Geological and Geophysical Information System (GGIS) that permits analysis and manipulation of satellite images, digital topography, geology, and seismicity on a single, multiple-window, computer screen for the interpretation of the tectonic and geomorphic setting of seismic events and their propagation paths to aid the possible verification of a CTBT or TTBT. The second objective

was to evaluate this system and methodology by performing morphotectonic analysis of tectonically active areas, especially central Asia. These test site investigations revealed needs for new analysis, combination, and visualization techniques for the datasets. New methodologies were then developed and implemented in the ongoing studies. The incremental development of the system in the course of evolving site studies was effective because problems encountered in early stages were resolved and useful new utilities were added progressively by modifying subsequent designs.

Morphotectonics is the extraction of tectonic information, such as the character and amount of recent deformation, from geomorphology. Currently available satellite images and digital topographic data are the primary source of regional morphotectonic information. Integration of topographic and image data with teleseismic and local-array seismicity, and other geophysical datasets, will permit the analysis of the tectonic setting of seismic events and their propagation paths. One main objective of our research was to investigate the character of available digital topographic and satellite image data and determine how best to use them for the interpretation of morphotectonics. We expanded our scope of the project to include digitization of geologic and tectonic information from maps into the GIS.

RESULTS

The following is a summary of our results of developing a practical methodology for effectively handling the diverse datasets of interest to DARPA's ongoing efforts in nuclear test ban treaty monitoring research. The large volumes of digital topography, satellite imagery, and geologic map data available for Central Asia and elsewhere necessitates special techniques to efficiently pro-

vide access to the data for analysis. Where possible, we have built upon commercial software packages, including IIS's System 600, Ithaca Software's HOOPS, and ESRI's ARC/INFO, to allow us to concentrate on developing methodologies and the acquisition of new datasets instead of the coding of low-level computer routines for the basic operations and user interfaces. We divide the different dataset types up in the discussion below for convenience.

Topography

A large and detailed dataset covering the whole area of Central Asia is digital topography. We have completed the processing of the large digital topography dataset (DTED level 1; ~100 m resolution; the level available to us) that we requested and have received from the Defense Mapping Agency (DMA) during 1989 and 1990, covering the high topography of the Himalayas, Tibet, the Hindu Kush, Pamirs, Tien Shan, Altai mountains, and Lake Baikal regions of Central Asia, including the Kazakhstan test site, plus a dataset that we received covering the southern part of Novaya Zemlya including the nuclear test site (Figure 1).

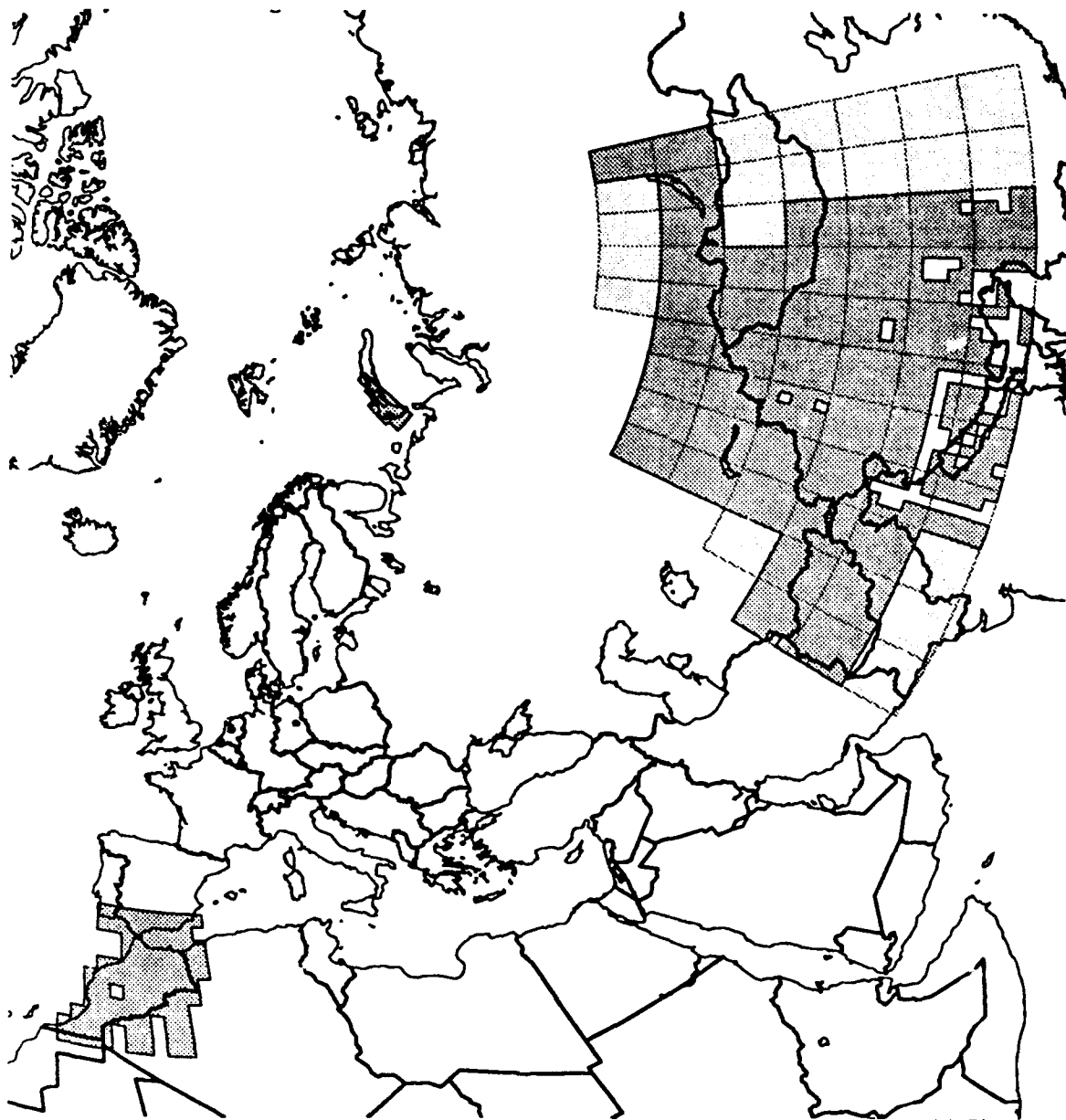
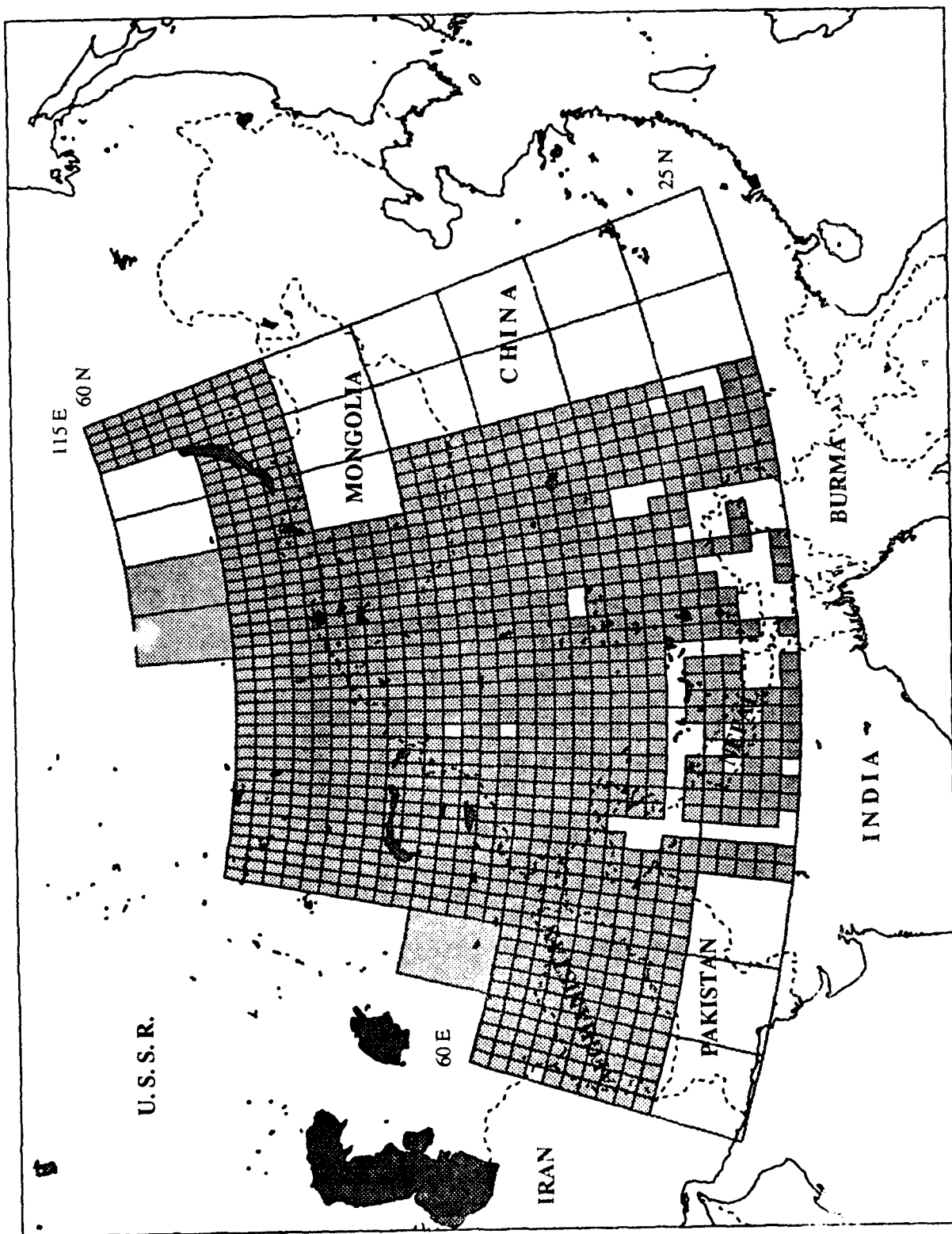


Figure 1. Map of Eurasia showing area covered by mosaics of digital topography for central Asia, Novaya Zemlya, Morocco and requested data. Coastlines are *black lines* and country borders are *dark gray lines*. DTED cells received during 1989, 1990, and 1991 are shown *filled medium gray with black outline*, cells received in 1991 that were not yet processed as of this report are *filled very light gray*, cells missing from the data are visible as *blank areas* between filled cells (Table 2). All 5° x 5° blocks are outlined by *medium gray lines*. Map is an azimuthal projection centered in north central Eurasia.

The dataset consists of 1090¹ "cells" for the central Asia data (see Figure 2) plus 23 cells for Novaya Zemlya and 89 cells for the Morocco area (see Table 1 and Figures 1, 11, and 12) that each cover a square degree with a spacing of 3 arc-seconds (1200 points per degree) in the latitude direction and in the longitude direction for the cells south of 50°N (DMA, 1986). At higher latitudes, the latitudinal resolution changes to six arc-seconds (600 points per degree) north of 50°N (including the northernmost part of the central Asia dataset and then to nine arc-seconds (400 points per degree) at 70°N (including the Novaya Zemlya dataset). We have converted our catalog of the locations of all the DTED cells, as well as our other geographic information into the ARC/INFO Geographic Information System (GIS; see Figures 1, 2, and 11). The standard processing sequence that converts and mosaics the DTED in file formats that we view and analyze on our workstations and image processors is described below.

Figure 2. Overview map of Central Asia showing coverage of DTED cells received. Received and processed cells (see Table 1) are shown *filled medium gray with black outline*, cells received but not yet processed are *filled light gray*, cells missing from the data requested are visible as *blank areas* between filled cells (Table 2). New 5° x 5° blocks requested for 1990, are outlined by *thick gray lines*. Country borders are shown as *thin black dashed lines*. Seas and major lakes are *filled gray with black borders*. Grey-scale and shaded-relief mosaics in Figures 3 and 4 cover entire area of processed cells. (Figure on facing page.)

¹ Another 466 new cells were received after January 1991. They are being processed.



**Table 1. Cornell Asia Topography Acquired¹ List
5° x 5° blocks**

lat., long. range	cells rec'd ²	geographic reference
27°-38°N, 12°W-0° * §	89 ‡	Morocco, Atlas and Rif mountains
25°-30°N, 75°-80°E	19	Delhi, Agra
25°-30°N, 80°-85°E	20	Kanpur, Annapurna
25°-30°N, 85°-90°E	15	Katmandu, Mt. Everest
25°-30°N, 90°-95°E †	11	Lhasa to Khasi Hills, Shillong
25°-30°N, 95°-100°E †	12	Myitkyina, N Burma
25°-30°N, 100°-105°E	21	K'un-ming, Minya Konka
30°-35°N, 65°-70°E	25	Kabul, central Afghanistan
30°-35°N, 70°-75°E	25	Peshawar, Islamabad, Lahore
30°-35°N, 75°-80°E	16	Dehra Dun, E Kashmir
30°-35°N, 80°-85°E	18	W Tibet, Lipu Lekh
30°-35°N, 85°-90°E	20	WC Tibet
30°-35°N, 90°-95°E	25	EC Tibet
30°-35°N, 95°-100°E *	19	Pa-tang, Ning Ting Shan
30°-35°N, 100°-105°E	24	Min Shan, Lin-t'an
35°-40°N, 60°-65°E	24	NW Afghanistan, Samarkand
35°-40°N, 65°-70°E	25	Dushanbe, NE Afghanistan
35°-40°N, 70°-75°E	25	Garm to Nanga Parbat
35°-40°N, 75°-80°E	25	W Tarim basin, Karakoram
35°-40°N, 80°-85°E	25	central Tarim, Tibet
35°-40°N, 85°-90°E	25	Tarim, central Altyn Tagh
35°-40°N, 90°-95°E	23	E Altyn Tagh
35°-40°N, 95°-100°E	25	W Nan Shan
35°-40°N, 100°-105°E	25	E Nan Shan, Lan-chou
40°-45°N, 65°-70°E *	25	E. Uzbekistan, W. Kirghizia
40°-45°N, 70°-75°E	25	W. Tien Shan, Frunze
40°-45°N, 75°-80°E	25	central Tien Shan, Alma-Ata
40°-45°N, 80°-85°E	23	E Tien Shan
40°-45°N, 85°-90°E	25	Turfan depression
40°-45°N, 90°-95°E	25	Lop Nor
40°-45°N, 95°-100°E	25	Yu-men, Gobi
40°-45°N, 100°-105°E	25	central Gobi
45°-50°N, 75°-80°E	25	E Balkhash, Taldy-Kurgan
45°-50°N, 80°-85°E	25	E Kazakhstan
45°-50°N, 85°-90°E	25	USSR-Mongolia-China border
45°-50°N, 90°-95°E	25	W Mongolia, Ulaangom
45°-50°N, 95°-100°E	25	Uliastay, central Mongolia

¹ As of March 1991.

² Full coverage for a block is 25 cells. Difference from 25 are missing cells that were "unavailable" from the DMA, leaving gaps in topography coverage.

* These data were received March 1991.

§ Note that this block is not 5° by 5°.

‡ There are 16 cells missing from this dataset (not including pure ocean cells for which data was not expected).

† We received the data for this block again, *with the same cells missing*, in March 1991.

50°–55°N, 80°–85°E	25	Semipalatinsk, almost Novosibirsk
50°–55°N, 85°–90°E	25	central Altay
50°–55°N, 90°–95°E	25	E Altay, Artemovsk
50°–55°N, 95°–100°E	25	Nizhneudinsk
50°–55°N, 100°–105°E	25	Irkutsk, SE Baikal
50°–55°N, 105°–110°E	25	Ulan-Ude, central Baikal
50°–55°N, 110°–115°E	25	Chita
55°–60°N, 90°–95°E *	25	Siberia
55°–60°N, 95°–100°E *	25	Siberia
55°–60°N, 110°–115°E	25	NE of Baikal, Bodaybo
70°–75°N, 51°–57°E ‡	23 ‡	southern Novaya Zemlya

We also requested digital topographic data for the area of the Central Andes in South America for which we have TM coverage. Our existing DEM for the Central Andes is on a 3' (~5 km) grid and was digitized by hand from the Operational Navigation Charts here at Cornell (see Isacks, 1988). We were informed that the data was unavailable. We also have a DEM that covers all of California with a ~150 m grid, approximately the same resolution as the DMA DTED Level 1. The U.S.G.S. sells DEM's for 7.5' quadrangles with a 30 m grid for some areas in the U.S. We acquired a few dozen of these high resolution datasets for widely scattered areas of the U.S. to compare with the DTED (described below under *Data Limitations*).

Processing

We have developed a standard processing sequence that converts the DTED into a form that can be viewed on workstations and image processors. This processing involves the reformatting of the data into the IIS (International Imaging Systems) System 600 file format that allows more rapid access to selectable areas of images. As the data was read in and processed, we mosaicked each 5° x 5° block of cells together into one file to allow larger areas to be exam-

* These data were received March 1991.

§ Note that this block is not 5° x 5°.

‡ There is one cell missing from the center of the southern part of Novaya Zemlya, other missing cells are ocean.

ined at various resolutions. The DTED mosaics were done both with the original elevation values (16 bit integer elevation in meters) and with values scaled to the more convenient for display 0-255 range (8 bit integers). The 5° x 5° degree blocks for the full resolution files appear to be a good tradeoff between viewing larger areas and making files that are of manageable size (36 MB for the 8-bit mosaics and 72 MB for the 16-bit versions for the DTED south of 50°N).

The next step in the processing, after the 5° x 5° degree mosaic files have been created, is the calculation of the mean, maximum, minimum, and total relief (max-min) for a set of different sized moving windows (from 20 x 20 to 600 x 600 points) applied to the full resolution data. As described in more detail below, these derived data sets can be used for the interpretation of surface roughness on a variety of scales for comparison to the propagation paths of L_g and the different climatic/erosion regimes in Central Asia. The calculations maintain the full range (maximums and minimums) of values in the original data but result in a more manageable dataset that can be stored on-line and manipulated for the whole area of coverage, *e.g.*, to generate topographic profiles along great-circle paths as described below under *Analysis*.

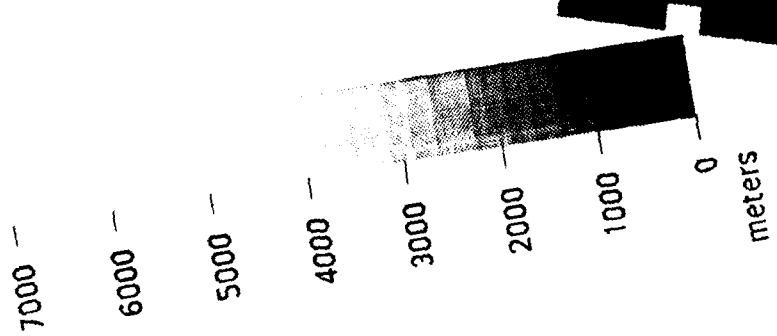
Visualization tools

We investigated several different visualization techniques for the processed topography data and evaluated the usefulness of each for analysis. The simplest method of viewing the topography is to assign a grey-scale value to the elevations running from black at the lowest elevations (usually near or at sea level) through grey shades to white at the highest elevations (which vary depending on the area). We used this type of grey-scale representation of the topography for "quick-look" evaluations of mosaics and map-projected mosaics both on the com-

puter screen and as hardcopy. Contrast stretches and rescaling can be applied to the data for a given area to produce enhanced grey-scale products. A program was written to generate PostScript™¹ for the grey-scale images that allows hardcopy printing on standard laser printers. We find that grey-scale images are very useful for producing figures that show relatively large-scale features and are easy reproduced with standard black-and-white photocopiers (Figure 3).

Figure 3. Grey-scale mosaic of Central Asia DTED cells processed. The original DTED was averaged over a 50 by 50 window to produce a Central Asia DEM mosaic. The mosaic was then projected into a Lambert Conformal Conic projection (~5 km resolution) that fits on one page and shows the major morphotectonic features. *White* shows areas of missing data: "not available" (small irregular holes) or not yet acquired (blocks at NW and SW corners of mosaic—see also Figure 2 and Table 2). Colors run from *white* at the lowest elevations through *black*, *dark gray*, and *medium gray* at low to moderate elevations (100m to 3 km above sea level) up to *light gray and white* at the 4–6 km high elevations of the Tibetan plateau, Tien Shan, Himalayas, Pamirs, Hindu Kush and other mountain ranges. The small areas of the highest peaks in the Himalayas and northern Tibet (above 7 km elevation) are shown as *black*. (Figure on next page.)

¹ TM of Adobe.

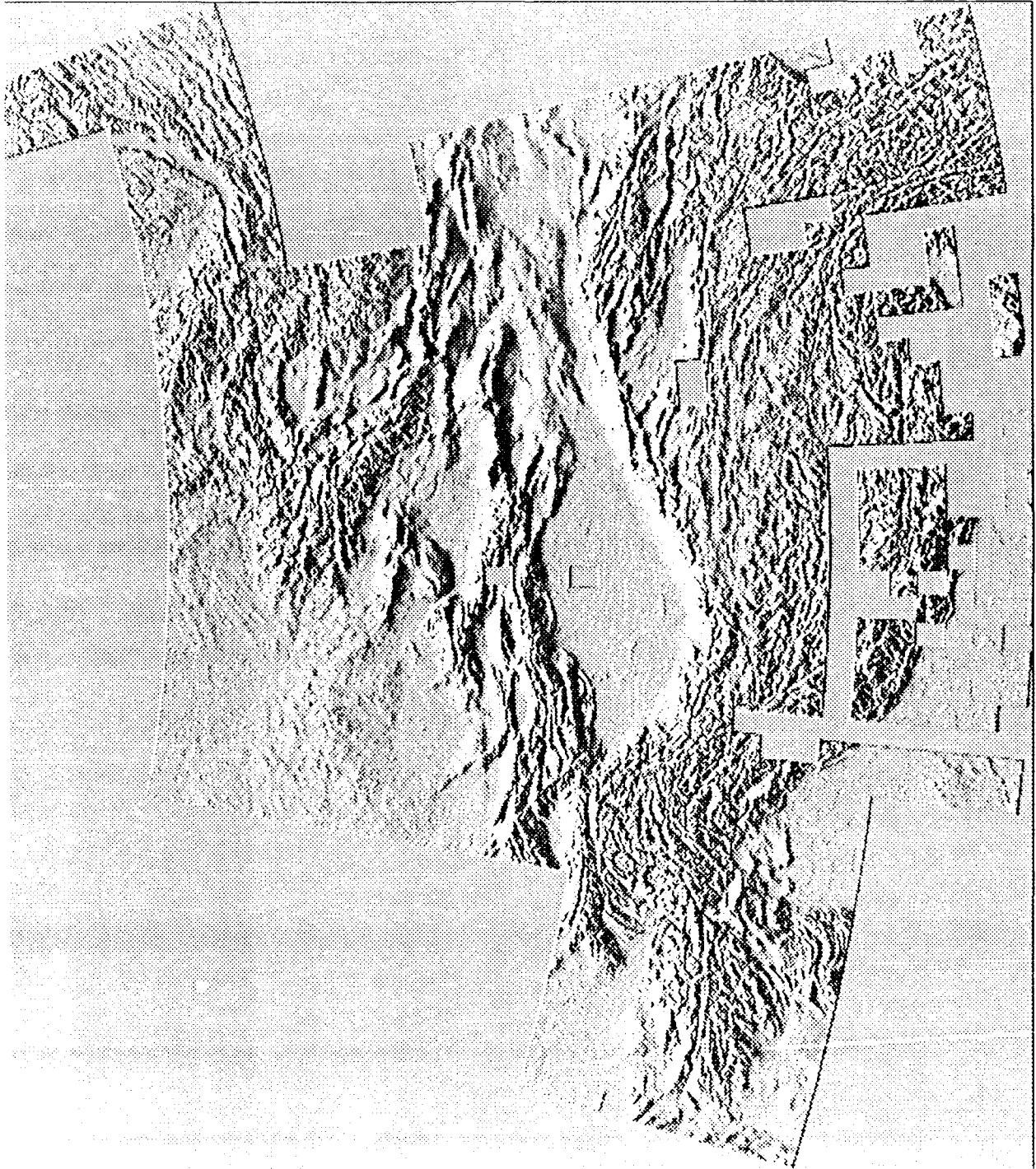


A more colorful method of portraying the data is by assigning pseudocolors to different elevation ranges. Typically up to 256 different colors are available on a given display, usually arranged in some kind of "rainbow" progression. We have designed two special pseudocolor scales that provide better contrast for topography data than the generic color scales that are part of the IIS System 600 software. We use one of our custom pseudocolor schemes extensively for displaying the topography both on the IIS displays and on workstation displays and hardcopy prints. Unfortunately, it is impractical to include color figures in this report due to the difficulties of reproducing color. Pseudocoloring is a very effective way of rendering the long-wavelength features in a topographic database, and it can easily be applied to large datasets such as the mosaics.

We found very useful the IIS System 600 "virtual roam" programs which pan a viewing window (1024 x 1024 or 512 x 512 pixels) across large images such as the ~1 km resolution mosaic that is more than 4000 pixels in both directions or the full resolution 5° blocks that are 6000 x 6000 pixels. Virtual roam also allows "zooming in" or enlargement of selected areas, as well as interactive rescaling and modification of the lookup table that assigns different gray shades to the gray-scale images, or colors to the elevations of the DTED images. This approach allows an analyst to examine subtle geomorphic features while still retaining a large field of view to provide a regional context for the topography. There is also a function within the roam programs that allows the drawing of graphic annotations, such as points, lines, text, polygons, or circles, on the image and the saving of these elements to a file. The graphics file can then be converted to ARC/INFO for combining with other geographic information in plots or maps, as discussed below.

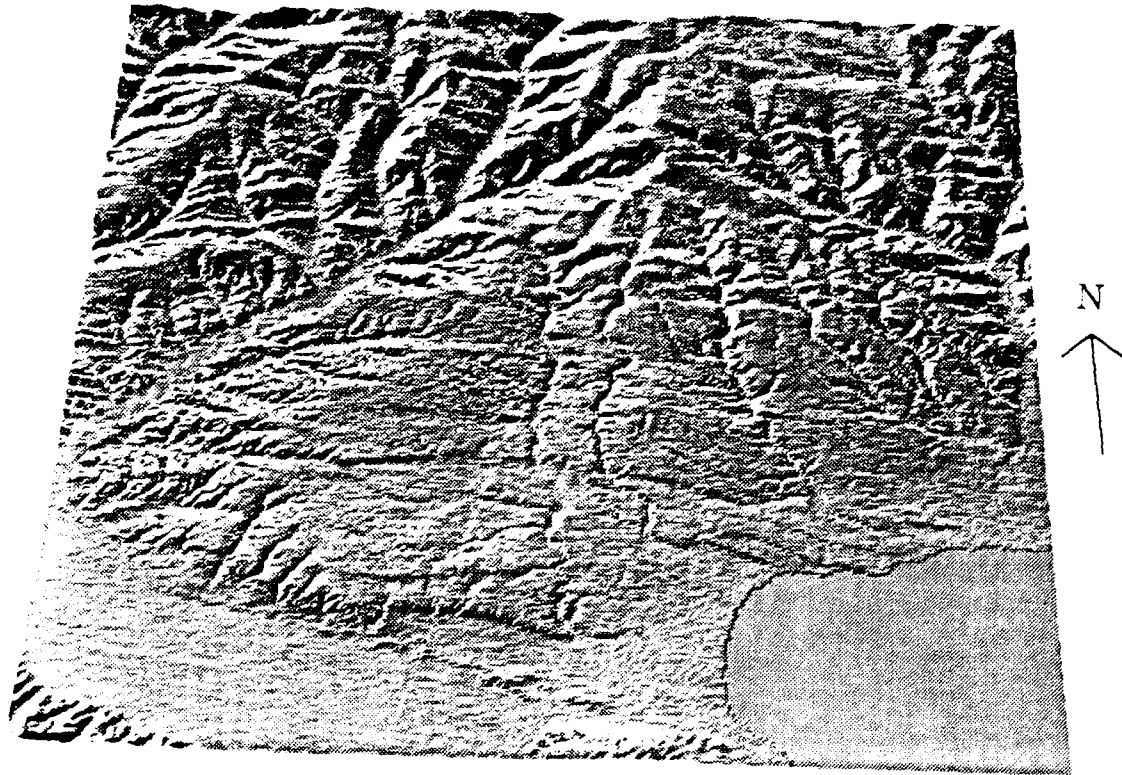
A new method of visualizing the moderate-size mosaic images is by rendering the data into a synthetic-stereo shaded-relief image with a "hill shade" program and a synthetic parallax generation program. The first part of this processing calculates the aspect of each point on the surface relative to a "sun" and shades that pixel accordingly (see Figure 4 for an example of a shaded-relief view). Then the elevation of each point of the DEM is used to calculate the appropriate relief displacement (or parallax shift) for each pixel of the shaded image to create a stereo pair mate. In the stereo pair, conveniently viewed as a red-blue anaglyph, one image is the shaded image (shown in red) and the mate (shown in blue) is the parallax-modified shaded image. This type of rendering has been called by some "2-1/2D" meaning that it is more than a 2D map, but not a full 3D perspective (which is computationally expensive for large DEMs). Viewing these synthetic stereo images is similar to viewing of SPOT stereo images (as described below), except that the amount of vertical exaggeration can be adjusted in the synthetic stereo images and the DTED (Level 1) have lower resolution than SPOT images and lack information on surface reflectance. In areas of varying relief, such as at the Himalayan front, it is sometimes necessary to calculate two versions of the synthetic stereo images with different amounts of vertical exaggeration. Lower exaggeration to view the high relief mountains, and a higher exaggeration version to see the details in the lower relief areas. We have produced shaded synthetic stereo images for all of the reduced-resolution mosaics and for all of the full-resolution 5° blocks.

Figure 4. Shaded relief rendering of Lambert projection 5 km resolution mosaic for Central Asia. Topography is vertically exaggerated and then illuminated by a light from azimuth 330° with an elevation of 30°. *Flat gray blocks* are areas of missing data: "not available" (small irregular holes), or not yet acquired (blocks at edges of mosaic). This shaded relief image can be combined with another that has synthetic relief displacement to view the topography in stereo, using either red and blue glasses or a stereo viewer. (Figure on next page.)



A more advanced visualization technique is simulating 3D perspective views with synthetic lighting to examine small- to moderate-scale topographic features, such as the scarps of active faults. We have written software to do the 3D visualization using the Ithaca Software HOOPS graphics package that runs on nearly every workstation and minicomputer system, including the VMS VAXstations and Ultrix DECstation that we use and the Sun SPARCstations in use at the CSS. This 3D "rendering" of the topographic data is much more computation-intensive but can show more details for the smallest features than the synthetic stereo images. This is because the parallax of the synthetic stereo images is quantified to integral multiples of a pixel so features with less than the amount of relief that corresponds to a pixel of parallax are lost. Active faults stand out in these 3D views, especially in more arid areas, such as central China and the area near Lake Baikal (see Figures 5 and 6). The resolution used for these 3D views of $1^\circ \times 1^\circ$ cells is 400 m, created by subsampling the original data by 4 to create a 300 x 300 grid of elevations. This is about the largest grid that can be easily rendered with our existing software and hardware, and the 400 m resolution largely ameliorates the effects of the digitization artifacts visible at the full 100 m resolution. This visualization technique enhances mesoscale morphotectonic features, especially those with a high degree of linearity. Large fault scarps formed by active faults stand out in these rendered views (Figures 5 and 6).

Central China faults in alluvial surface



SE corner of cell 37 N 99 E
Horizontal resolution = 200 m
Vertical exaggeration = 2.0

Camera at -100, 35, 160 km
Light at 1.5, 1.0, 0.5

20 km

Figure 5. Synthetic 3D perspective view looking from south to the north showing a system of faults to the east of Tibet in the Nan Shan of central China. Location of the $1^{\circ} \times 1^{\circ}$ cell, rendered with a "light" from the north, of the DTED is at 37°N , 99°E . The southeast quarter of the cell was subsampled by 2 from the full resolution of the data producing a grid with approximately 200 m resolution. Vertical exaggeration of a factor of two was applied.

Analysis

Geomorphic interpretation of surfaces using digital topography and satellite imagery in an area can yield useful information on the long-term fault activity in the absence of detailed ground mapping. We developed a set of criteria for interpreting the effects of varying climate on the interpretation of fault activity; for example, the central part of Tibet and the entire Gobi and Takla Makan (Tarim

basin) deserts have low precipitation (almost all less than 300 mm/year) so we would expect low erosion rates and good preservation of active or recently faults. Indeed we can see clear evidence for the Neogene strike-slip and normal faults mapped by the Geotraverse team in Tibet (see discussion of the digitization of this database under *Digital Map Datasets* below). The lack of evidence for faults in other arid areas can be used to infer a lack of Neogene fault activity in those areas.

Diagnostic geomorphic features, such as pressure ridges, offsets in river channels, and scarps in alluvial fans (e.g., Figure 6), are visible on active (likely to have Quaternary displacement) faults when the full resolution topography is rendered into stereo shaded-relief views. These faults are mapped on the image processor screen and their coordinates are saved to a file. This file is then converted into ARC/INFO for comparison with previously mapped faults and recorded seismicity. The new stereo "virtual roam" capability allows an analyst to scan for features over a large area quickly, and the synthetic stereo portrays much of the third dimension while still maintaining the geographic fidelity of a map view. Particularly interesting features can be rendered into 3D perspective views that better show the surface, but cannot be used for mapping (e.g. Figures 5 and 6). The smaller faults in the alluvial fan at the SE of Figure 5 are not on existing maps, showing the usefulness of interpreting the topography for adding to previous geologic information. This surface appears to be geomorphically young, so the faults that cut it are likely to be active. The locations of larger faults, such as the normal fault that bounds the north side of the graben in Figure 6 (mapped as "active" by Trifonov, 1986), can be much more accurately located on the DTED than on published small-scale maps (1:8,000,000 in this case).

Zmax = 2973 meters
Horizontal resolution = 400 meters
Vertical Exag. = 3.0
Cell 51°N 102°E

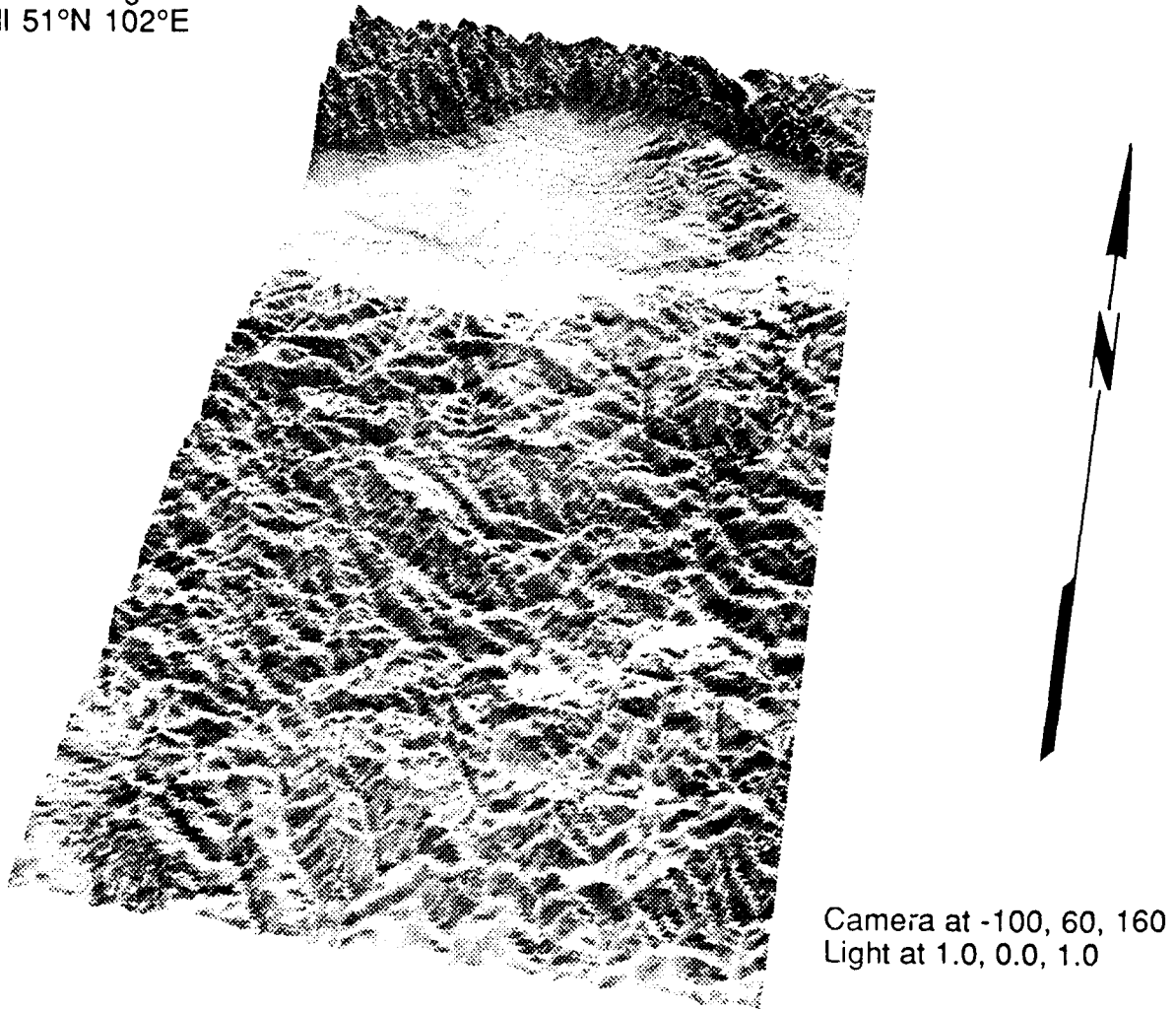


Figure 6. Synthetic 3D perspective view like that of Figure 5, showing part of the active normal fault system near Lake Baikal. Location of this cell of the DTED, also rendered with light from the north, is with SW corner at 51°N, 102°E.

We investigated ways to calculate roughness from the full resolution topography data. One useful and straightforward method, which we made part of our standard processing sequence as described above, is to move a window over the data and calculate the mean elevation and range of relief (maximum minus minimum elevation) within the window. The roughness images, calculated on the 5° x 5° blocks are then mosaicked together to cover the entire area (see Figure 7).

These images show that relief varies greatly in Central Asia from flat alluvial basins (relief near zero) to dissected high mountains (relief of 1000–4500 meters). The Tien Shan of Tadjikistan, Kirghizia and western China has relief of greater than 1000 m, over a 10 km wavelength, for much of its length and width (Figure 7), with a maximum relief of over 3000 m. The Himalayan front along the southern edge of the Tibetan Plateau and much of the northern edge have high to very high relief surrounding the plateau, with much wider zones of high relief at the western end, in the Pamirs and Hindu Kush, and at the eastern end, south-central China. In general the high relief regions correspond to areas where the precipitation and fluvial and glacial erosion are significant. The arid central part of Tibet has very low relief, comparable to some low elevation areas, despite its ~4.8 km average elevation.

Figure 7. Gray-scale mosaic of surface roughness calculated from the Central Asia DTED. Roughness is measured as relief (maximum – minimum elevation) within overlapping 100 x 100 windows (on the same grid as the mean values of Figure 3). This ~5 km resolution mosaic has been projected into the Lambert Conformal Conic projection. *Thin white lines* are 5° grid lines for geographic reference. *White* shows areas of missing data and very low relief in the flat alluvial plains and lake surfaces. Regions of high relief in the Tien Shan, Pamirs, Himalaya and elsewhere may block the propagation of high-frequency L_g waves. Gray-scale bar shows relief values.

(Figure on facing page.)



3000 —

2000 —

1000 —

0

meters

Several qualitative studies have noted the lack of propagation of high-frequency L_g waves across major mountain ranges, such as the Central Andes (Chinn, Isacks, and Barazangi, 1980), Himalaya–Pamirs (Ni and Barazangi, 1983), Turkish and Iranian Plateaus (Kadinsky-Cade, Barazangi, Oliver, and Isacks, 1981) and other ranges in Central Asia (Ruzaikan, and others, 1977). Extreme surface roughness caused by fluvial and glacial erosion may significantly contribute to explaining the lack of propagation across high mountain ranges. Use of L_g amplitudes along such paths for discrimination or yield estimation could be invalid or require correction factors. The surface roughness images can be used to map out areas of significant relief. The calculated maximum and minimum value images maintain the full range of the original data but result in a more manageable dataset that can be stored on-line and manipulated for the whole area of coverage to generate topographic profiles along great-circle paths (see Figures 8 and 9). These profiles of topography in a swath along the propagation path of L_g from a given event show the amount of topographic relief at the surface that could contribute to scattering high-frequency energy.

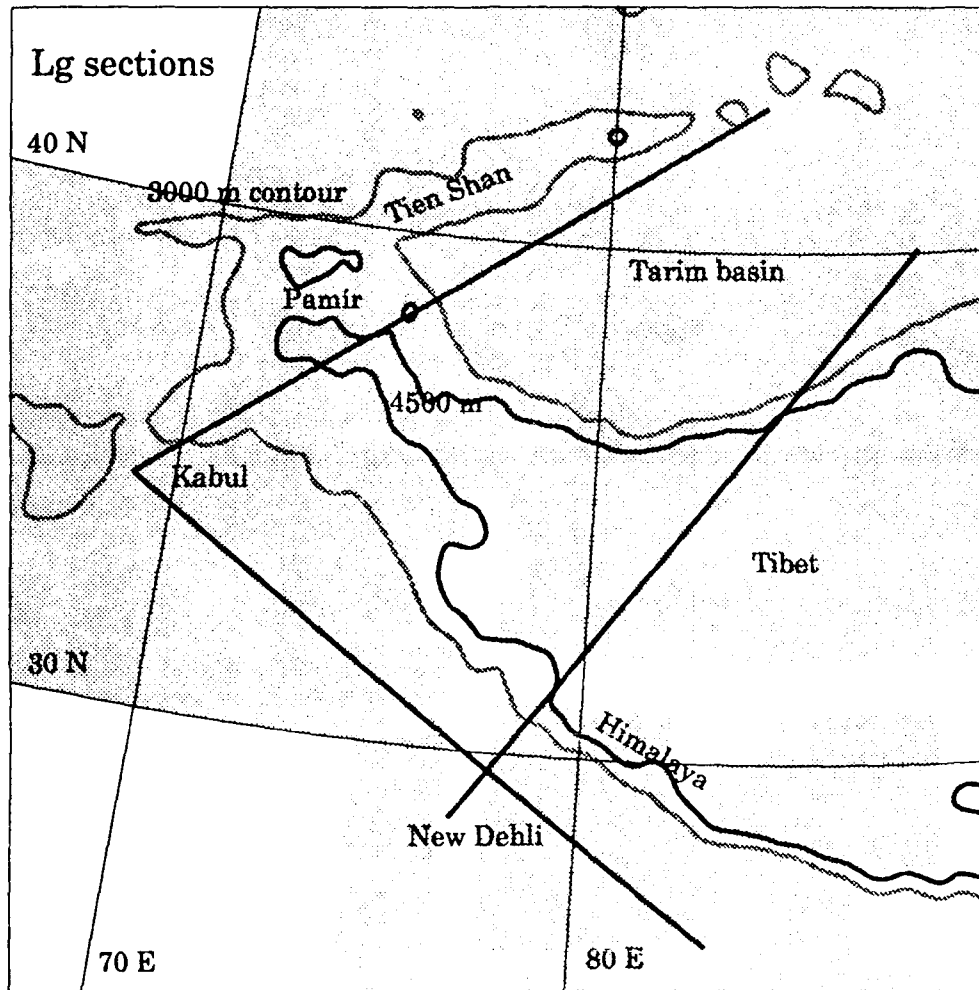


Figure 8. Map showing locations of L_g propagation paths for which the topographic profiles are shown in Figure 9. Light gray fill shows coverage of received DTED cells. Thin black lines mark 10° latitude and longitude lines. Contours on smoothed version of the topography are shown as thick light gray line for the 3000 m contour and thick dark gray line for the 4500 m contour. Great circle paths marking the centers of the swaths of the topographic profiles are shown as thick gray lines from Kabul and New Dehli. Paths crossing the high topography of the Himalayan front and the Pamirs were found to destroy high-frequency L_g phases (Ni and Barazangi, 1983).

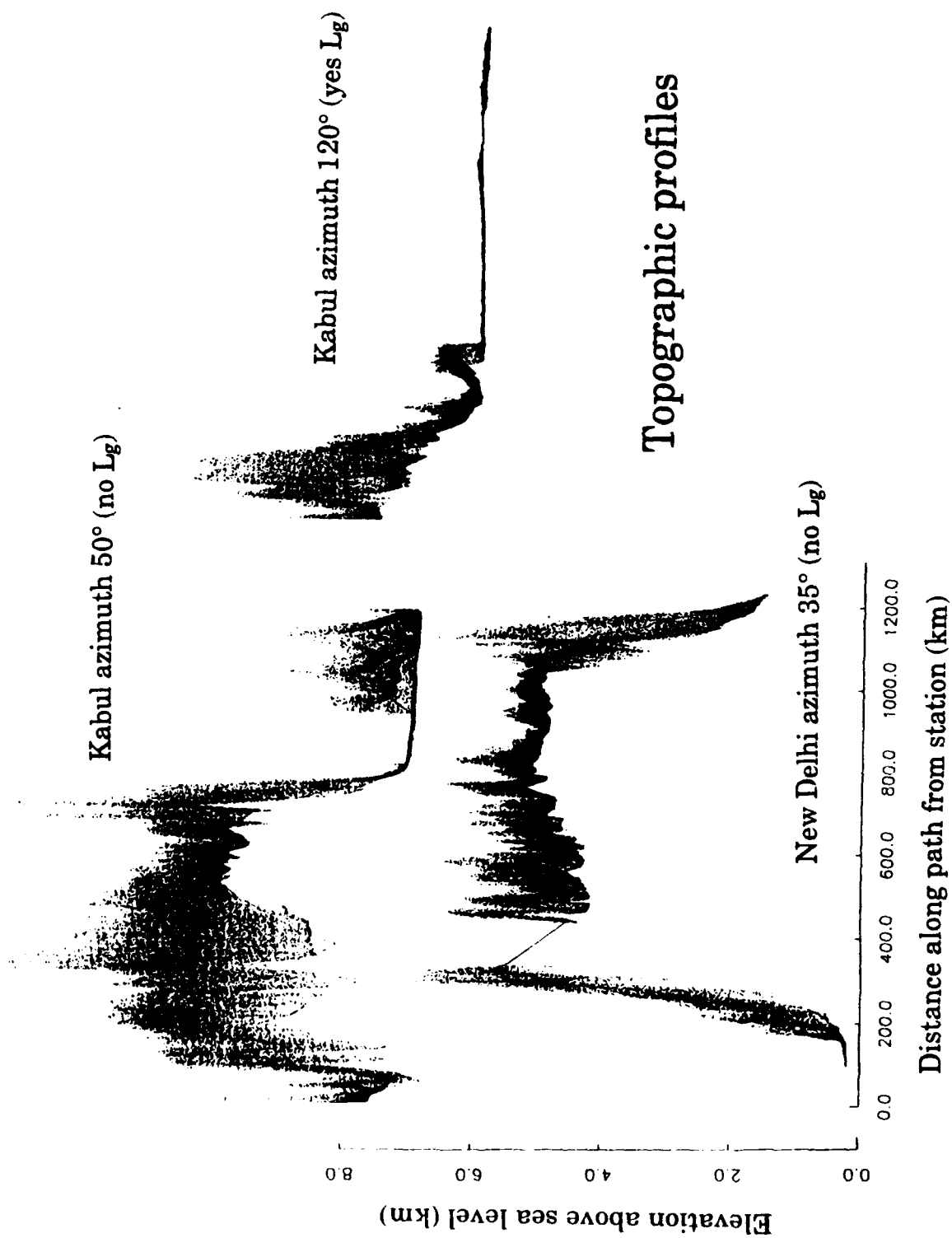


Figure 9. Topographic profiles along swaths centered on great circle paths of L_g propagation as shown in Figure 8. Each swath is 50 km wide, and *points* (maximum and minimum elevations within 2 km windows) are projected into the plane of the

great circle. Profiles are all at the same scale, with a large amount of vertical exaggeration, as seen in the elevation and distance scales plotted at the left and bottom, respectively. Noted is whether L_g propagates efficiently along the path of each profile.

Both satellite images (e.g., SPOT and Landsat Thematic Mapper—TM) and Digital Elevation Models (DEMs, also called Digital Terrain Elevation Data, DTED, by the DMA) are now available for various parts of the earth at spatial resolutions or grid spacings that vary by about three orders of magnitude, from 10 m to over 10 km. There is a trade-off between the sample spacing and areal coverage of digital topography, with the coarsest resolution (10 km) data available for the entire earth. The effective spatial resolution is not necessarily as high as the grid spacing of the dataset, but depends on the resolution and accuracy of the source (contour maps, airphotos, satellite images, or altimeters), the digitization method used, and the subsequent error correction and resampling. All topographic digitization methods result in varying degrees of degradation of the source spatial resolution. Digitization artifacts introduce errors that must be quantified in order to effectively interpret the data set. Moreover, the optimal spatial resolution of a DEM or image depends on the scale of the morphotectonic problem being studied. The highest resolution data can be used for local studies, while regional topographic datasets, with wider grid spacings, are useful for orogen-scale analyses (e.g., Isacks, 1988). An optimal GIS must be capable of manipulating multiple resolution datasets to allow the interpretation of various scales of structures.

Data Limitations: Gaps, Artifacts, and Resolution

A significant problem with the DTED that we received is the numerous cells for which the data is missing (Table 2; Figures 1 and 2). As we put together our mosaic of the DTED cells (Figure 3), we found that the data holes due to DTED

cells that we did not receive from the DMA make it difficult to get a complete picture of the high topographic relief along the Himalayan front and to study southern Tibet and other areas with holes. The wording on our transmittal from the DMA is "all cells requested but not shipped are unavailable". We submitted a formal request through the GL to fill in the holes and received the data for two blocks in March 1991 with the same cells missing (Table 1), so we conclude that the DTED still does not exist for these cells at this time.

Table 2. Cornell Asia Topography List of Missing Cells for Data Acquired

25°N 77–78°E¹
25°N 81°E
25°N 88°E
25°N 90–91°E
25°N 95–97°E
26°N 77°E
26°N 86–97°E
27°N 77°E
27°N 84°E
27°N 86–88°E
27°N 90–93°E
27°N 97°E
27°N 103–104°E
28°N 77°E
28°N 81°E
28°N 83°E
28°N 88°E
28°N 92–93°E
28°N 95–97°E
28°N 104°E
29°N 77°E
29°N 82°E
29°N 93°E
29°N 95–97°E
29°N 104°E
30°N 77°E
30°N 82–83°E
30°N 88°E
30°N 95°E
30°N 103°E

¹ See Table 1 for geographic references for these cells.

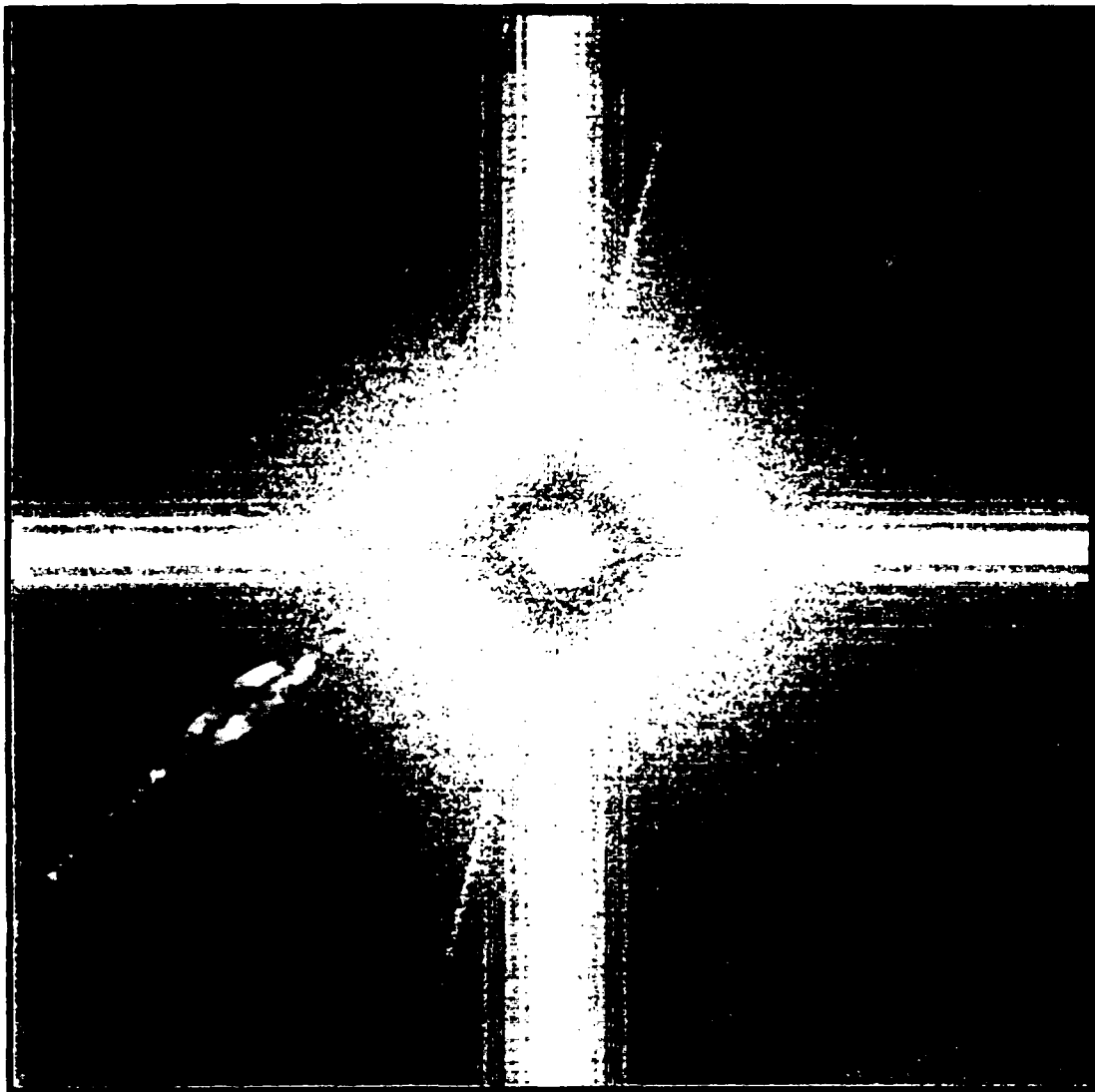
31°N 77–88°E
31°N 98°E
32°N 76–77°E
32°N 97–98°E
33°N 76–77°E
33°N 97–98°E
34°N 77°E
36°N 60°E
36°N 91–92°E
40°N 83°E
43°N 83°E

Analysis of the DTED cells shows the widespread presence of relatively minor errors or artifacts in the data. The two obvious artifacts are a “grain” visible at the highest resolution of the data, and mis-matched join lines that are visible at lower resolution. Both the original data source and method of digitization contribute to these systematic errors. The “grain” is probably due to human digitization of stereo photographs or imagery using an automatic-scan stereoplotter, as described below. The mis-matched join lines are likely due to inconsistent map sources or poorly aligned stereomodels. The join lines occur both at the boundaries between cells, and within cells. Elevation mismatches range from about 10 m to over 50 m.

The most common data source for DEMs is stereo photographs or images. Elevation data can be extracted from a stereo pair of images directly on a regular grid either by human or computer correlation of the surface features, but these techniques are relatively new. Human digitization of stereo photographs or imagery has been commonly done using an automatic-scan stereoplotter. These systems are set up to automatically scan back and forth across the stereomodel while the operator attempts to keep a “floating dot” on the surface. The inherent time lag in the operator's response to a change in slope, combined with the reversed direction of adjacent scans causes a systematic artifact in the digitized topography visible as a “grain” in the data at full resolution.

The degree to which the finest details can be studied with the stereo shaded-relief and pseudocolor roaming and 3D perspective techniques is limited primarily by the digitization artifacts of the DTED. We find that the human perception system can often distinguish the characteristic "grain" that is due to the artifacts from the high-frequency topographic features of interest, especially in the pseudocolor, grey-scale and synthetic stereo renderings. The 3D views can tend to enhance the "grain" of the artifacts unless the "sun" direction is chosen to be more or less parallel to the grain. The digitization artifacts often have a characteristic expression in a 2D power spectrum of the topography (Figure 10), with the power of the artifact sometimes highly localized along a narrow line in wave-number-wavenumber space. We investigated the possibility of filtering out the artifacts in the frequency domain by reducing the power along the line of the artifact to the level of the rest of the topography and then doing an inverse Fourier transform, but we found that this technique could only be applied to limited areas where the artifacts were especially coherent. Spatial domain filters such as a convolution with a 1 x 5 smoothing filter are fairly effective in reducing the artifacts, but also tend to destroy some of the higher frequency information.

Figure 10. Grey-scale two dimensional Fourier power spectrum of a 512x512 pixel portion of the DTED near latitude 55°N and longitude 110°E. The amplitude has been colored in grey levels from dark at the lowest power to light at the highest in a non-linear scale to enhance the features. The zero frequency ("DC" term) is at the center of the plot, with longitude spatial frequency ranging from -Nyquist to +Nyquist (600 cycles degree⁻¹ or ~5 cycles km⁻¹) along the horizontal axis and latitude spatial frequency similarly along the vertical axis. The digitization artifacts show up clearly as increased power along a diagonal line on this 2D FFT (which "wraps around" in the spectrum). We explored the possibility of filtering out these artifacts in the Fourier domain. (Figure on next page.)



We processed a set of DTED cells covering the southern part of Novaya Zemlya that we obtained as copies of data requested by another DARPA researcher (see Figures 11 and 12). The locations and outlines of the cells have been entered into our Arc/Info database, as shown in Figures 1 and 11. The Novaya Zemlya DTED cells, while not covering a large part of Eurasia, do cover the Soviet nuclear test site at Matochkin Shar.

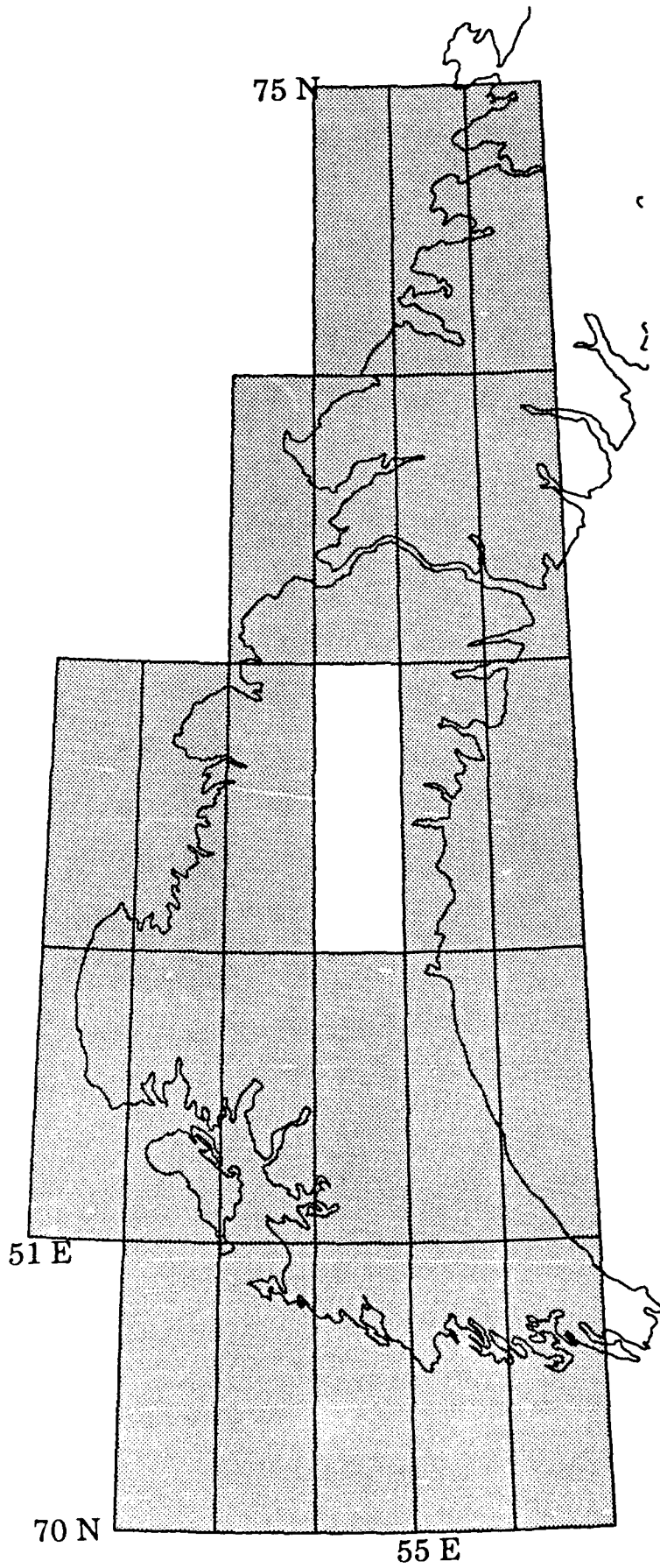


Figure 11. Map of DTED cells covering the southwest part of Novaya Zemlya. DTED at this latitude has only 400 points per degree in the longitudinal direction. White rectangle in middle is missing "unavailable" data.

The quality of these data, as evaluated qualitatively by viewing the full resolution data in pseudocolor mode, is not as good as most of the other DTED that we received for Central Asia. There are significantly more obvious artifacts in the data almost everywhere and there is a conspicuous bad join line between cells at the southern end of the island (visible even on the reduced by 7 resolution image of Figure 12 as a vertical discontinuity line). It is also unfortunate that there is a missing cell in the center of the southern part of Novaya Zemlya.

To investigate the information content of higher resolution data, we studied some USGS DEMs from the United States that cover 7.5' (0.125°) by 7.5' on a 30 m grid. These 7.5' DEMs have a higher resolution but are generally only available for limited areas so they cannot be used for regional interpretations. USGS 7.5' DEMs are classified as "level 1" DEMs, meaning they have not been corrected to make sure that adjacent maps join correctly, to remove systematic errors, or to make hydrographic features such as rivers, lakes, ridge crests, and islands continuous and correctly located (USGS, 1986; 1987). The DMA DTED from Asia is classified by the USGS as "level 3", meaning that adjacent cells will match exactly, systematic errors have been removed, and hydrographic features are correctly portrayed at a scale of 1:250,000 (DMA, 1986; USGS, 1987), although some digitization artifacts remain. Vertical resolution of the DTED data is 1 m, but the vertical accuracy is much lower, on the order of 50 m.

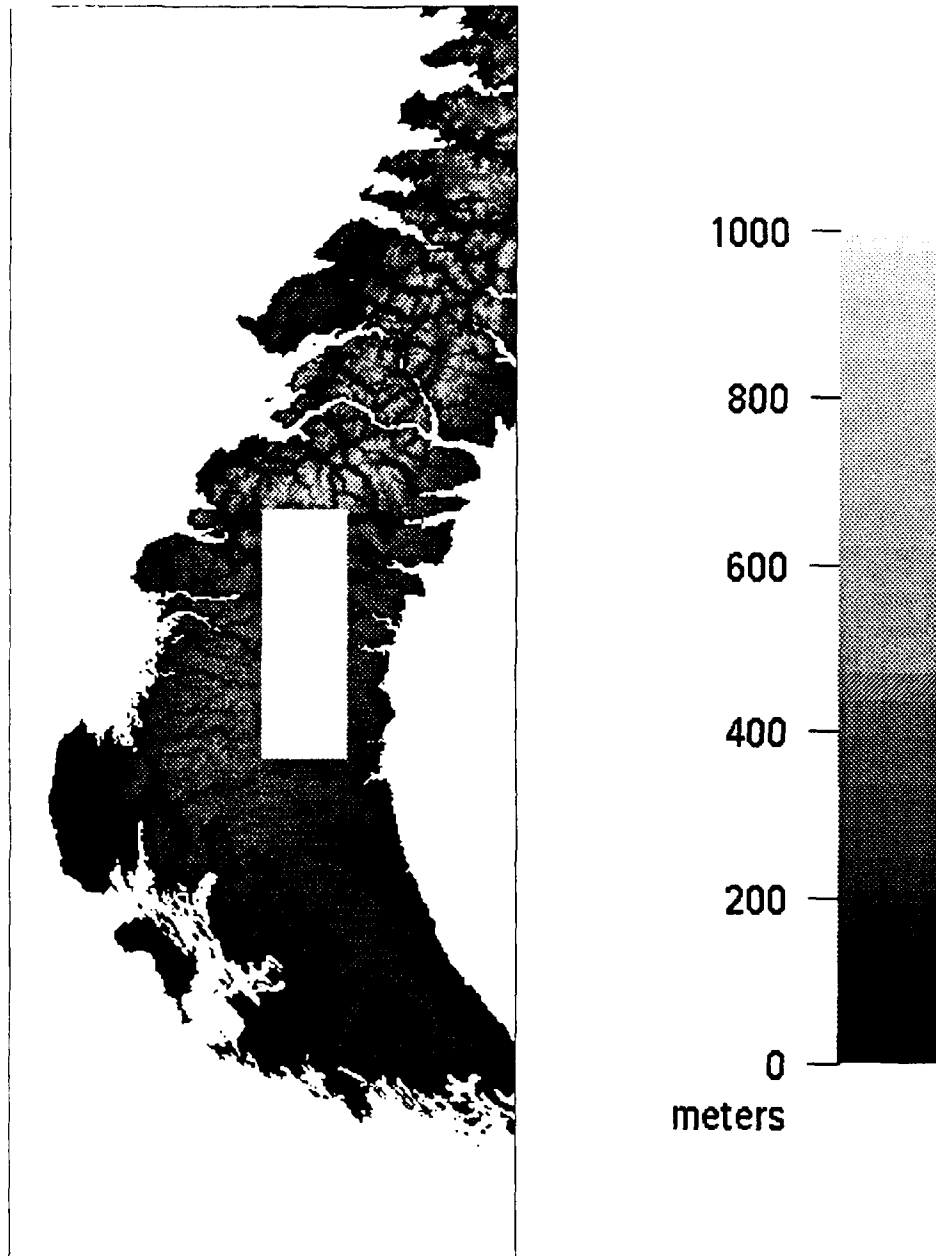


Figure 12. Gray-scale mosaic of DTED cells covering the southwest part of Novaya Zemlya. Data has been subsampled by 10 from the full resolution to about 1 km resolution. Area of coverage is shown on Figures 1 and 11. *White rectangle* in middle is missing "unavailable" data. Grey-scale bar shows elevations in meters. Note the vertical line near the southeast end of the island where there is a discontinuity between cells.

Study of varying horizontal resolutions of DEMs from North and South America and the DMA DTED from Central Asia shows that the minimum spatial

resolution necessary for the accurate interpretation of a morphotectonic feature such as a fault-generated mountain block depends on the degree of erosion, the amount of offset, and the along-strike length of the structure. An active, little eroded mountain bounding fault with significant offset and length can be detected on a DEM with an effective spatial resolution as crude as 5–10 points across the width of the uplifted block (about 500 m to 10 km for large structures), while accurate identification of the type and age of the underlying faulting requires data with at least 50–100 points per structure wavelength (25–500 m resolution). This indicates that efficient interpretation of topography for the tectonics and seismic potential of an area will require relatively high resolution DEMs, such as the DMA DTED data (~100 m grid) or higher resolution DEMs derived from stereo SPOT images (10–30 m grid).

Geological and Geophysical Data

We have created an extensive digital tectonic database by the digitizing of geologic, tectonic, and other maps for Central Asia. The data are organized into a hierarchical database of information from different resolution sources. In addition, “metadata” was collected about existing maps to create a database about what areas each map covers and where the hardcopy map is located. A new methodology for the digitization of faults with attributes such as their ages and for the polygon information on geological maps has been developed.

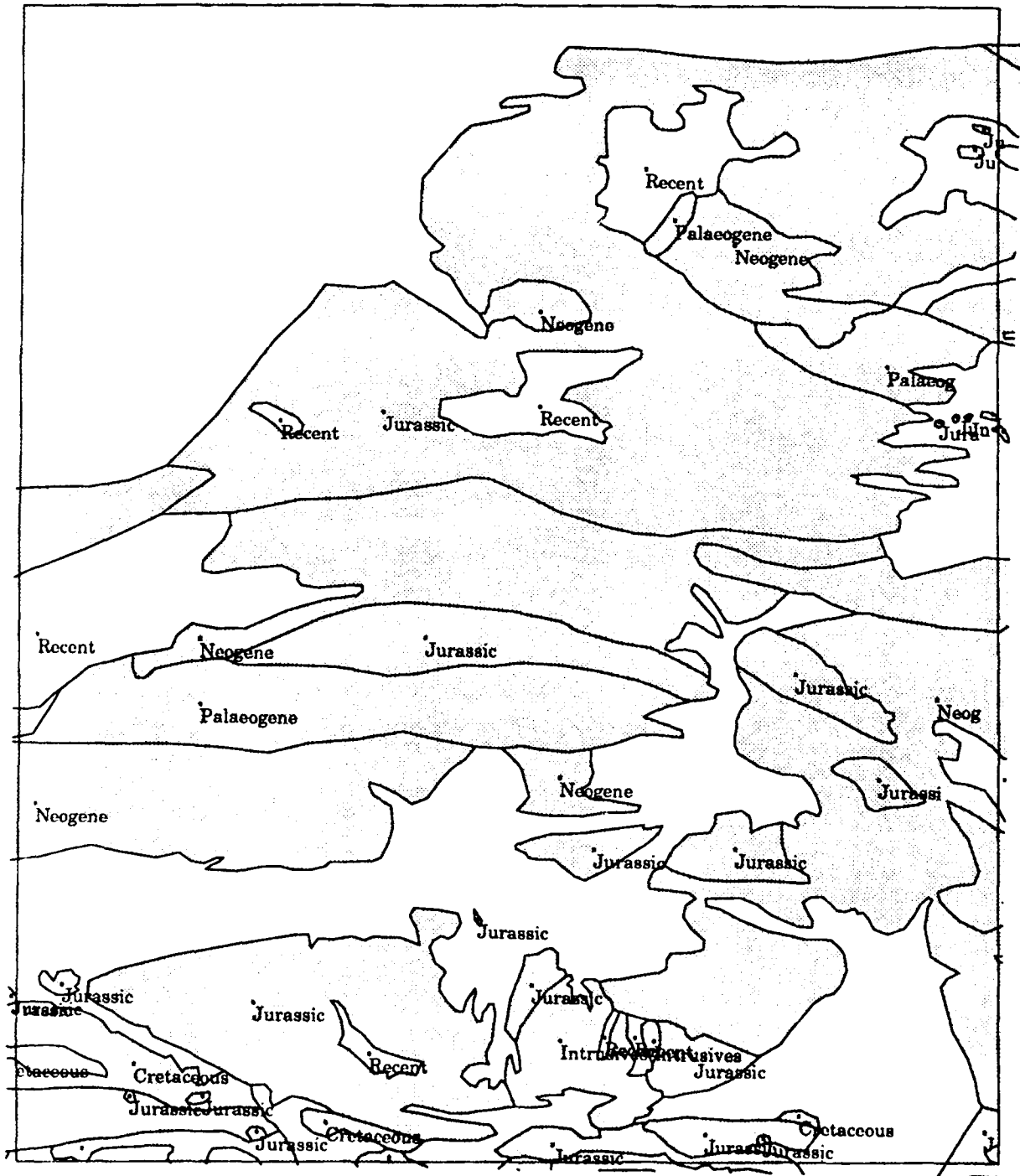
Technique Development

We used ARC/INFO, an advanced GIS package (acquired under a different project from ESRI, Environmental Systems Research Institute, Inc.), running on one of our VMS VAXstations. This package, along with our existing IIS System 600 image processing software including its ARC/INFO translator module, com-

pletely replaced a patchwork of different computer mapping file formats and programs. The ARC/INFO system is based on the INFO database management software, and can be modified to link directly into ORACLE databases (as used at the Center for Seismic Studies) as well. The ARC map digitization, editing, and plotting software is a well-integrated and powerful "toolbox" of components that can perform middle-level tasks. We have built a system for organizing geological and geophysical information using the ARC/INFO tools.

We converted all of our previously varied formats of geographic information files into ARC/INFO, and we have digitized geologic and tectonic maps for Central Asia. The new capability of ARC/INFO to maintain "attributes" associated with particular lines or polygons allows us to keep track of the fault type (normal, reverse, strike-slip, or unknown) and age category for the faults or to keep attributes for the age and compositional type for rock units. These attributes can then be used to assign different symbols on a map (see Figures 13, 14, and 16) or to select only a certain age category or fault type for plotting. ARC/INFO also maintains the topological information contained in a map of classified polygons or areas, such as a geologic map to allow the filling of polygons of a given type. Other research was done to perfect the use of ARC/INFO's "transform" and "project" programs to do the inverse map projections necessary to convert locations of features on a map in that map's projection to locations in geographic coordinates or latitude and longitude on the earth.

Figure 13. Map showing a detail of one degree square (32–33°N, 90–91°E) of the digitized geology coverage of the Geotraverse across Tibet (enlarged from the top center of Figure 16 below). All geologic units, except "Recent" alluvium are *filled light gray*. The labels of the individual polygons are shown as *small black squares*, with the unit age attribute printed below. This figure shows how the attribute data is associated with the polygonal boundaries of the units. Overlain are the boundaries of the one degree cell as *thin dark gray lines*. Map is a Lambert Conformal Conic projection. (Figure on next page.)



We developed a methodology for the digitizing of polygon as opposed to line data (as previously used for faults and contour lines) to digitize maps with areal

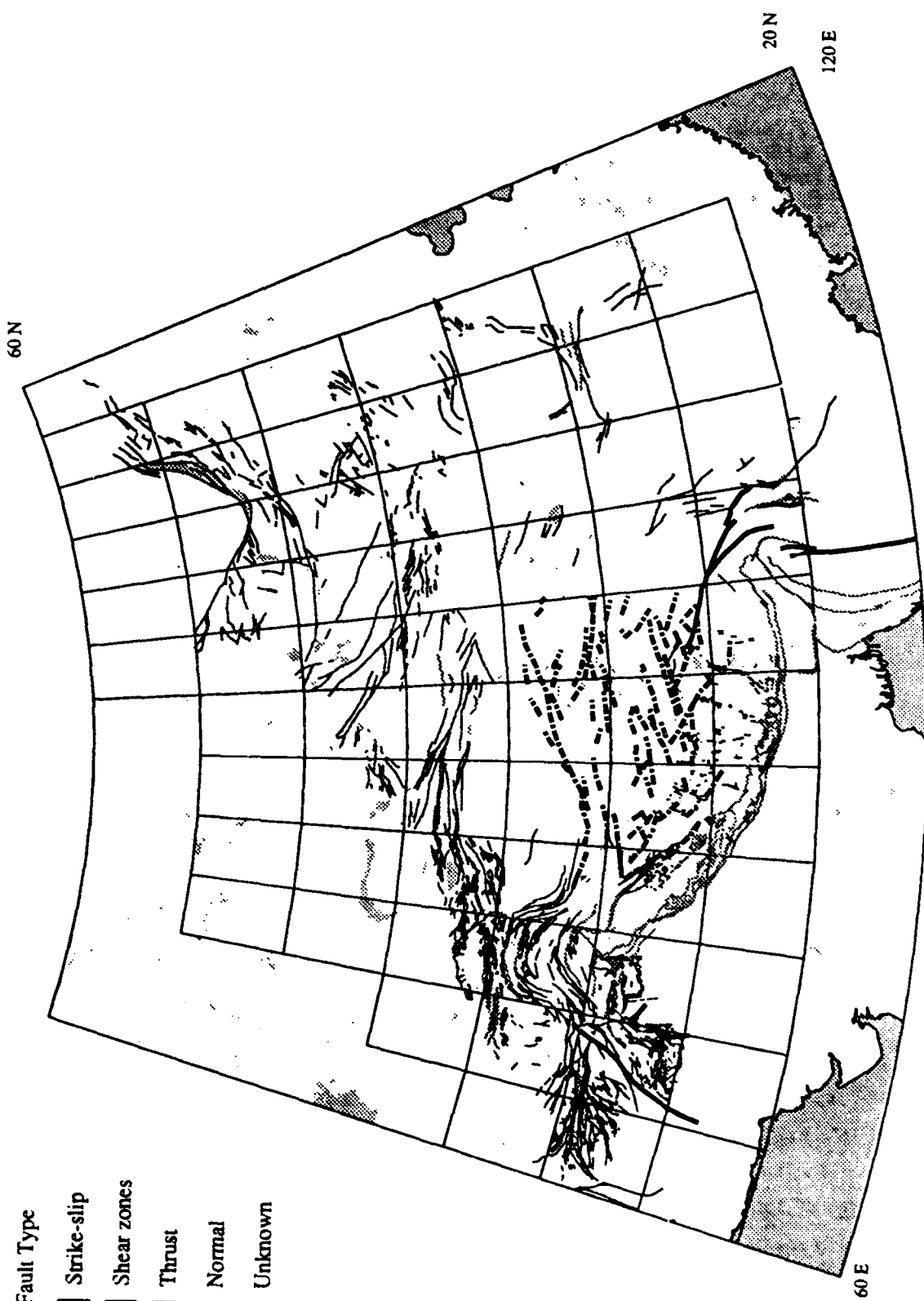
units, such as geologic maps. The lines or "arcs" marking the boundaries between geologic units are digitized along with a "label" point for each geologic unit. Then the arcs are formed into polygons that each enclosed one unit. Polygons are assigned two or more "attributes" within ARC/INFO via their labels that include information on the interpreted age and type of rock for the unit. These attributes allow one to select rock units of a certain age and then color or otherwise mark the different rock units on a workstation display or on a hardcopy map (see Figures 13 and 16).

Another ARC/INFO module, TIN (after Triangular Irregular Networks), has many useful capabilities for manipulating data sampled on regular or irregular grids, including topography, gravity, crustal or sedimentary basin thicknesses, or contoured rainfall datasets. Data can be contoured in any map projection, at any scale; converted from irregular to regular grids and vice-versa; or viewed in three-dimensional perspective views with any ARC/INFO dataset "draped" over the topography. We have developed programs to convert the DTED and other DEMs into the ARC/INFO TIN format, which allows resampling of the data points into a map projection, and also directly into a "lattice", their term for a regularly spaced grid with a header that defines its spatial attributes, including the corner of the lattice and the spacing between the points. The lattices can then be smoothed and contoured to produce contours on maps like those of Figures 8, 15, and 17. A disadvantage of the implementation of lattice files in the present version (5.0.1) of ARC/INFO is that they are limited to a maximum of 1024 points in any direction, so not even a full degree square (1200 x 1200 points) of the DTED data can be put into a lattice right now, but they have promised to remove this limitation in the next release.

Macro programs for ARC/INFO (in the ARC Macro Language—AML) were developed to enhance access to all of our databases (described in the next section), especially to better combine data of different resolutions or map scale. ARC/INFO macro programs allow the generation of menus and mouse selection of options or map objects for a user-friendly interface that will work the same on all of the graphics terminals and workstations on which ARC/INFO runs. The AML programs are also useful for selecting data and plotting them with a given map projection and symbols. The ARC/INFO pictures here were produced with AML programs that also serve to record the exact datasets, symbols, and projections used.

Digital Map Datasets

We converted all of our previously varied formats of geographic information files into ARC/INFO, and we digitized several geologic and tectonic maps for Central Asia directly into ARC/INFO. The first step was the digitization of the major known faults for the entire area of Central Asia covered by the DTED acquired (Figure 14). The attribute ARC/INFO capability was used to record the fault type (normal, reverse, strike-slip, or unknown) and age category for the faults, and to record the map source for each fault. These attributes can then be used to assign different symbols on a map (see Figure 14) or to select only a certain age category or fault type for plotting. Most of maps used for this overview database have a 1:2,000,000 scale or smaller



Fault Type

-  Strike-slip
-  Shear zones
-  Thrust
-  Normal
-  Unknown

Figure 14. Small-scale overview map of published Late Cenozoic faults in Central Asia, digitized and integrated into ARC/INFO. This map covers same area as Figure 2. Lakes, seas, and ocean are *filled light gray*. Requested and acquired 5°x5° blocks are marked with *solid black lines*. Each fault has a "fault-type" attribute that was used to assign different line types in this plot as shown in the key: *double solid black lines* for strike-slip faults and shear zones, *thick gray lines* for thrust faults, *thin black lines* for normal faults, and *thin medium gray lines* for faults of unknown type (where the fault type was not marked on map from which it was digitized). (Figure on previous page.)

We digitized one area of Central Asia where there is a relatively detailed geologic map to compare with the digital topography, the "Geotraverse" along the only major road across Tibet (Kidd, 1988; Kidd and others, 1988). This 1:500,000 scale map is the most detailed available for any complete section across the plateau (see Figure G). The wide variety of tectonic and geologic units from Paleozoic rocks and faults to Mesozoic deposits and sutures to active normal faults, combined with the arid to semi-arid climate made this an excellent place to calibrate our methodology. The topographic data along this section is relatively complete (almost no missing DTED cells within the area of the map) compared to other sections across the plateau.



Figure 15. Map showing location of the digitized geology coverage of the Geotraverse across Tibet (*thick black line*) on a background of tectonic features of Tibet. The 3000 m smoothed contour is *filled light gray*, and the 4500 m contour is *filled medium gray*. *Thick gray lines* mark positions of sutures between the tectonic terranes of Tibet, interpreted from the outcrops of ultramafic rocks and major fault zones. *Triangles* mark locations of young volcanoes and *circles with crosses* mark calderas. The *hatched area* is the area of S_n attenuation mapped by Ni and Barazangi in northern Tibet. The outline of the available DTED (same as on Figures 1 and 2) is a *thin black line*. Map is a Lambert Conformal Conic projection.

The integration of available vector datasets with the pseudocolor roam, rendering, and stereopair roam of the raster topography and images is leading to improved visualization of and insight into morphotectonic features that can bear on nuclear test discrimination and detection and the propagation paths of crustal and lithospheric phases. We concentrated on the digitization of the geologic units from the southern half of the "Geotraverse" map (see Figures 15 and 16).

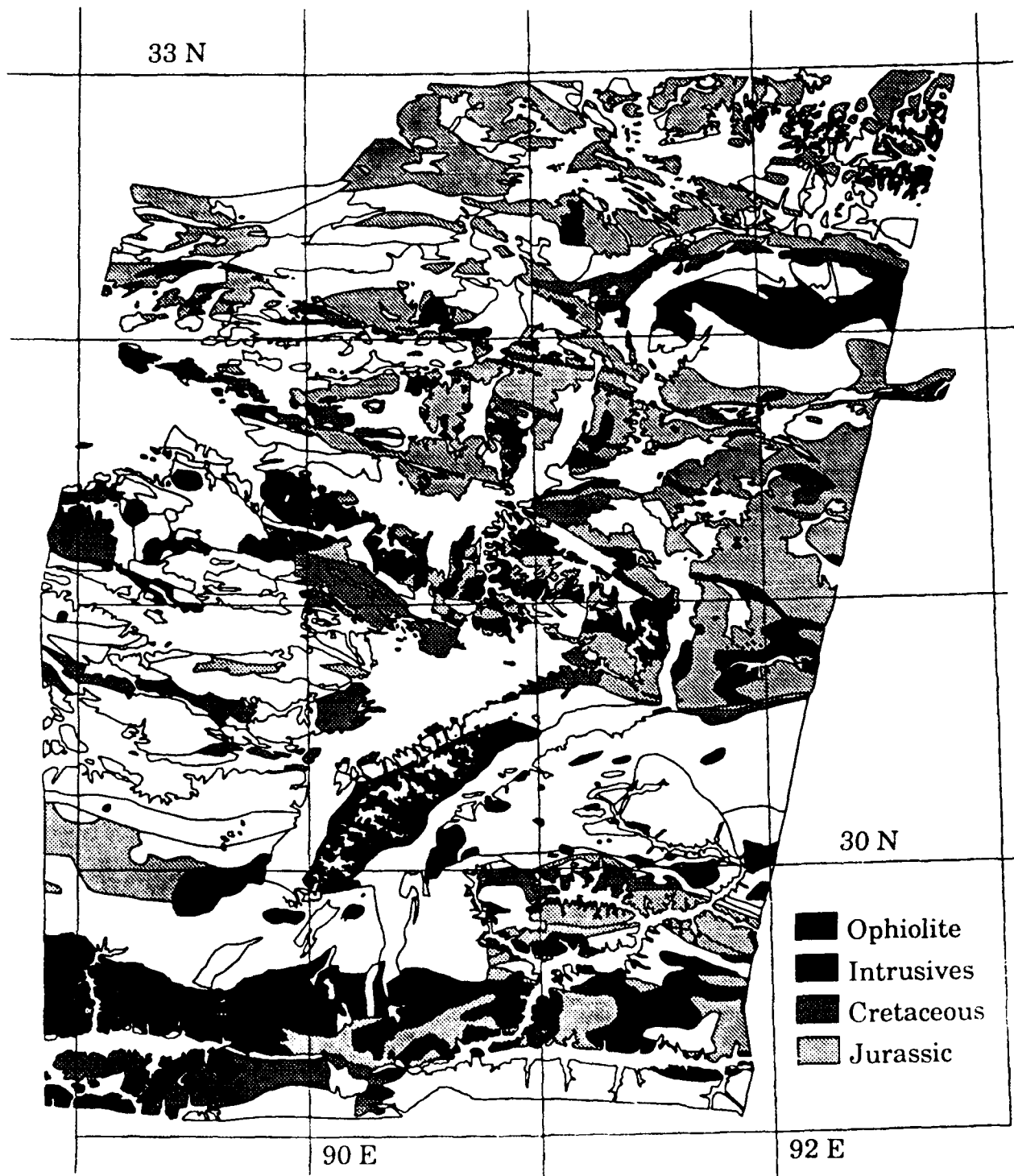


Figure 16. Map showing the digitized geology coverage of the southern half of Geotraverse across Tibet (see Figure 15 for location). Four geologic units are filled with grays according to the key. Overlain are the boundaries of the available topographic data as thin dark gray lines. This map contains more than one thousand individual polygons, each with attributes of unit age and rock type (see Figure 13). Map is a Lambert Conformal Conic projection.

We digitized some basic climatic information for Central Asia into our ARC/INFO database, especially annual precipitation (Figure 17). The zones of high precipitation (> 1000 mm/year) are areas where we would predict that fault scarps and other geomorphic features associated with faults will be eroded and erased much more quickly than in drier areas. Conversely, in the extensive dry areas where annual precipitation is less than 300 mm, we expect that manifestations of faulting should be clearly visible if deformation has occurred in geologically recent times.

We also acquired a set of maps of the entire Soviet Union with a variety of different kinds of geological and geophysical information at a scale of approximately 1:7,500,000. The maps of crustal thicknesses (depth to Moho) and sedimentary basin depths (isopachs) are probably the most useful. The attributes capability of ARC/INFO, can record which contours are dashed (inferred or interpolated) and which are solid. After digitization and subsequent editing, regularly spaced grids of the crustal and sediment thickness values can be created from these preliminary maps.

We completed our digitizing of basic climatic information for Central Asia into our Arc/Info database, including annual precipitation (Figure 17), river runoff and water evaporation rates. The zones of high precipitation (> 1000 mm/year) are areas where we would predict that fault scarps and other geomorphic features associated with faults will be eroded and erased much more quickly than in drier areas. Conversely, in the extensive dry areas where annual precipitation is less than 300 mm, we expect that manifestations of faulting should be clearly visible if deformation has occurred in geologically recent times.

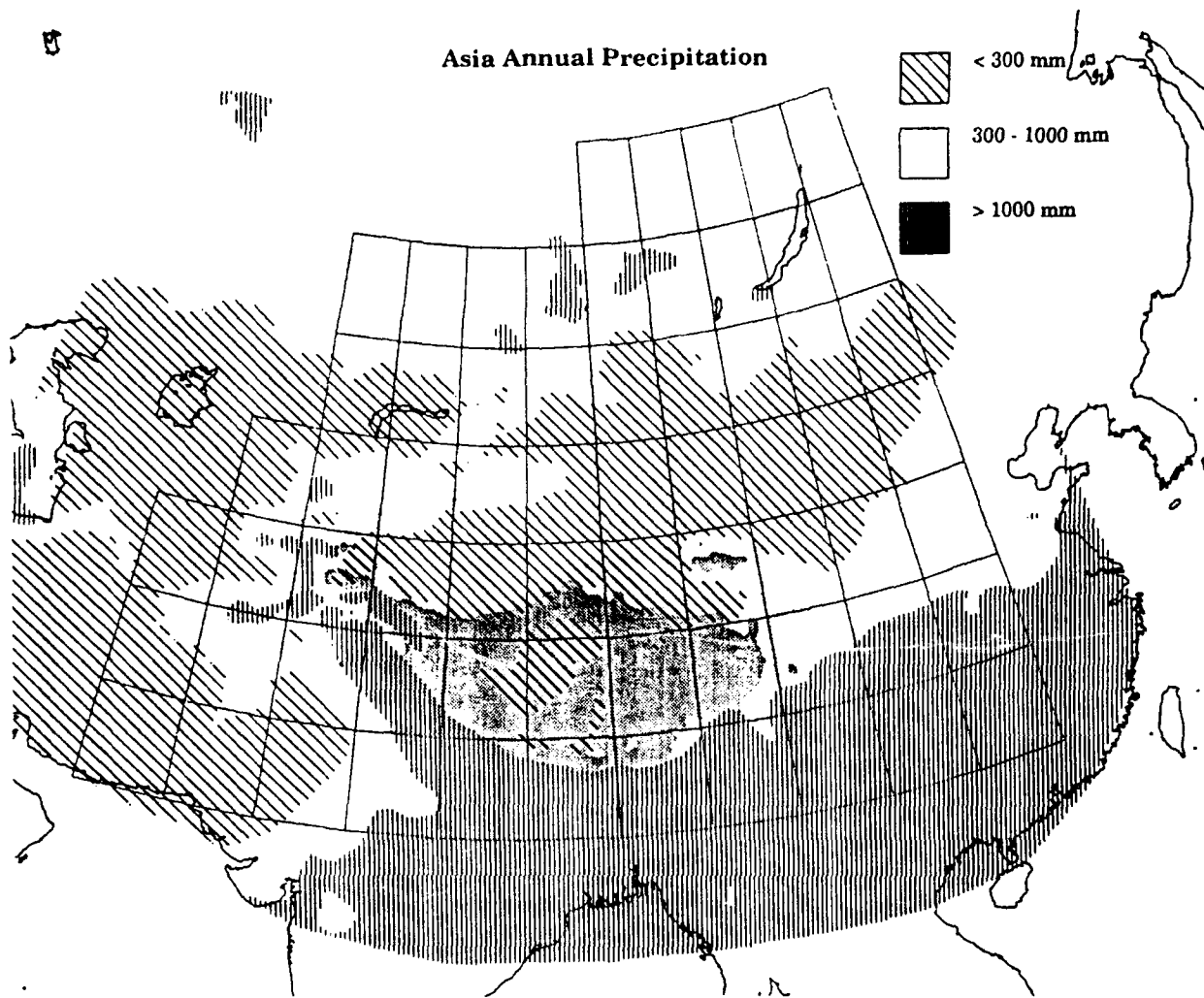


Figure 17. Map of annual precipitation and topography for Central Asia, produced with ARC/INFO. Map covers same area as Figure 2, and has the same 5° x 5° outlines of the requested and received DTED data blocks. Coastlines, seas, and major lakes are marked by *narrow black solid lines*. Smoothed topography is shown by *light gray fill* for areas above 3 km and *medium gray fill* for areas above 4.5 km. *Hatchure patterns* show smoothed contours of annual precipitation, as marked in the key. Moderate precipitation values between 300 and 1000 mm/year are *not hatchured areas*. Note the correlation between the areas of high precipitation and the areas of extreme surface roughness on Figure 7.

We entered the published locations of 93 Soviet nuclear tests (Vergino, 1989) and all their associated attributes into ARC/INFO. This allows one to use the graphical query capability of ARC/INFO to click a mouse on a given event and see all the information about that event. The relational database part of ARC/INFO also allows the selection of events for plotting based on any combina-

tion of criteria from the attributes. We converted the standard digital ISC (International Seismology Center) and PDE (Preliminary Determination of Epicenter) catalogs of seismic events into Arc/Info format, including all of the attributes associated with the events, such as location, depth, date, time, number of stations used, magnitudes, etc. This allows us to overlay these events and dynamically select events from the Info relational database for drawing on working plots on the workstation screen or making hardcopy maps such as Figure 4 or make graphical queries.

Satellite Imagery

An excellent source of high-resolution information about remote and inaccessible areas, such as central Asia, is satellite imagery. We have concentrated our research on the evaluation of SPOT imagery because it offers the highest resolution available commercially (unclassified) in digital form. We also took advantage of our large collection of Landsat Thematic Mapper imagery for South America to evaluate the relative utility of the different types of data.

SPOT

We received a total of eight SPOT scenes for Central Asia under this project (each half of a stereopair; see Table 3). We have processed the raw data into images that can be viewed on our International Imaging Systems (IIS) IVAS display (which is the same full-color image display that is used at the Center for Seismic Studies). We have added the new SPOT scenes to our ARC/INFO database of information about the previous SPOT scenes that we have received for Central Asia. The database includes the K and J indexes that SPOT uses to roughly locate scenes, the scene acquisition date, incidence angle and direction, center, and corner locations, and the location of the sun when the scene was

acquired (see Table 3 and Figure 5). We are still waiting for the stereopair mates for two of the requested scenes as of 18 March 1991 (Table 4). Apparently the weather in these areas prevented acquisition during the 1990 season.

Table 3. Cornell SPOT Central Asia Imagery Acquired¹ List

K	J	Inc. ang. & dir.	Acquis. date	Center lat. and long.		Sun azim. & elev.	
187	272	L16.1	08/07/89	38.815	70.393	146.0	64.7
187	272	R26.9	09/19/89	38.815	70.363	151.2	49.4
215	277	L17.2	08/27/90	36.367	83.363	150.7	61.3
215	277	R15.2	08/28/90	36.367	83.345	142.7	58.9
188	272	L13.7	09/09/90	38.815	70.983	157.7	54.9
188	272	R11.8	09/15/90	38.815	70.954	153.7	51.7
198	279	R12.1	11/07/90	35.387	74.764	163.3	36.9
194	268	R23.1	09/16/90	40.766	74.519	153.0	49.1

¹ As of March 1991.

Figure 18. Map showing coverage of SPOT scenes acquired for Central Asia. Outlines of the scenes that we have received are shown by *solid black lines* (see Table 3 for more data on scenes). The location of the IRIS/IDA digital seismic station GAR in the city of Garm is shown with a *square with an X*. Seismic events selected from the PDE catalog with $m_b > 3.5$ and depth < 50 km are marked by *medium gray crosses*. Topographic contours of smoothed topography form the background. *Filled light gray* is 3000 m contour, *filled medium gray* is 4500 m contour (see Figure 17). Map is a Lambert Conformal Conic projection. (Figure on next page.)

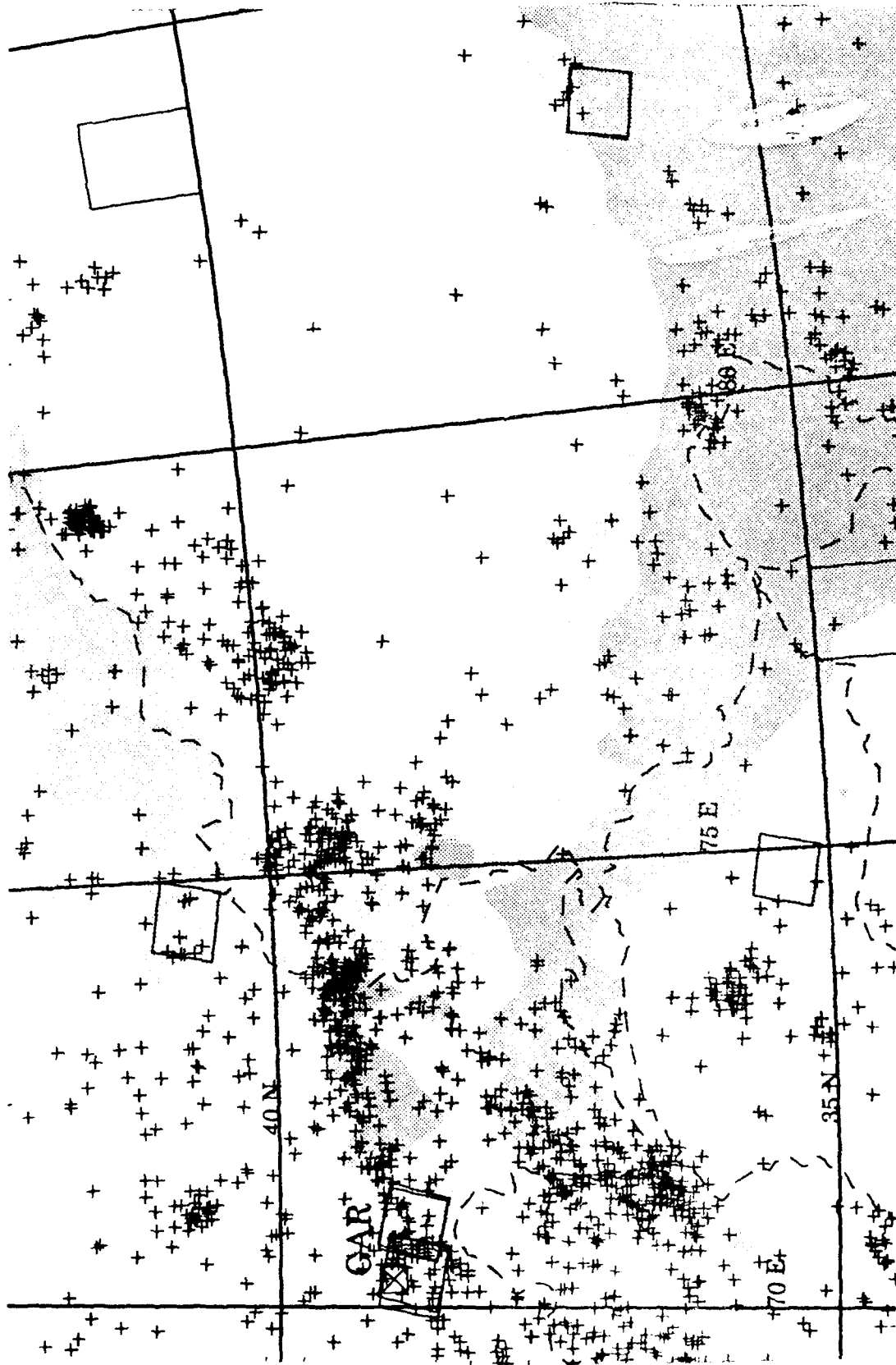


Table 4. Cornell Satellite Imagery 1990 Outstanding¹ Request List

satellite	scene specification	geographic reference
SPOT	left look ² K=194, J=268	Fergana fault, Tien Shan, Kirghizia
SPOT	left look K=198, J=279	Nanga Parbat, Himalaya, Pakistan

The scenes are of excellent quality with few or no clouds and snow covering only the highest elevations that are presumably always covered with snow. Figure 19 shows a reduced resolution image of the Nanga Parbat scenes. The extremely high elevations and relief of the Nanga Parbat mountain range in the K 198 J 279 scene (Figure 19) cause some very long shadows on the north-facing slopes which are in part caused by the lower sun angle at the November acquisition date (Table 3). The scenes are panchromatic (black-and-white) with 10 m resolution. We are still waiting for the stereopair mates for these two scenes. The acquired scenes were collected when the satellite was at points to the east or "right" of the ground area, so the other scenes need to be collected from points to the west or "left" (Table 4). It is probably not possible to get pairs of images that were acquired within a few days of each other (in order to have little change in their solar illumination geometry or in the ground features for better correlation between the images) since these areas are very often cloud covered, in fact we were unable to acquire cloud-free scenes to complete the stereopairs during the 1990 season.

¹ As of March 1991, we have received only one half of each of these stereopairs. Listed are the remaining two stereopair "mates". See Table 3 for the acquired images.

² Stereopair mates for previously acquired right looks (Table 3) should be panchromatic scenes acquired with incidence angles of about 10–20° left to form a stereo image with about 25–30° of convergence.



Figure 19. SPOT image of area around Nanga Parbat, Pakistan. Panchromatic image has been subsampled by 8.5 and contrast-enhanced. *White areas* are snow on mountain peaks. Many *dark patches* are shadows of high relief terrain. Peak of Nanga Parbat (elevation more than 8 km) is in SW corner of image. Sun illumination is from the southeast. This image was acquired from the right with an incidence angle of about 12° on 11/07/90. See Table 3 for more information. This is one of the scenes mapped on Figure 18. North is to the left on the image. Copyright 1990 SPOT Image Corporation.

The most exciting approach that we have adapted for real-time 3D visualization is to exploit the topographic information inherent in stereopairs of satellite imagery. Photogrammetric analysis has been applied to aerial photographs using opto-mechanical stereoplotters for more than 40 years, to produce the majority of topographic maps in use today. We have formed digital stereomodels from our SPOT stereo images. This process requires co-registering the two images in a common coordinate system in such a way that the parallax, or topographic relief displacement, is in the horizontal (X) direction. The stereopair can then be displayed as an anaglyph (the image from the right is in red and the image from the left in cyan or blue). One can then view the stereomodel on a conventional display by wearing red-blue glasses. The IIS System 600 software can be used to "virtual roam" over the stereomodel enabling an analyst to visualize both the topographic relief and the variations in surface reflectance shown by the images simultaneously.

We acquired five stereopairs of SPOT scenes for selected sites in South America (see Table 5) to evaluate their use in tectonic mapping and feature evaluation in areas where we have much more extensive ground information and an extensive library of Landsat TM imagery for comparisons. SPOT imagery of central Bolivian mines was compared to our TM imagery to evaluate the relative efficiency of the two data sets for locating and distinguishing active mining zones that are often the sites of large chemical explosions. The SPOT stereopair of the area around Jujuy, Argentina was studied for evidence of active faulting in an area where we have excellent local digital seismic network coverage. We also received four SPOT scenes (two panchromatic stereo pairs) from the San Juan, Argentina area, one of our three study areas, to compare with local array seismicity data (some 100,000 events were recorded by a local digital network in this

area) and mapped faults. We also used our set of Large Format Camera stereo photographs for the San Juan taken by the Space Shuttle to compare with the SPOT image pairs. The two stereo pairs cover adjacent (E-W) areas to the west and east of the city of San Juan, both with approximate latitudinal limits of 31°10'S to 31°40'S, and covering the approximate longitudinal limits of 68°20'W to 69°30'W. The two images for each of the pairs have look angle differences of about 30-40 degrees between them.

Table 5. Cornell SPOT Imagery for South America Acquired List

satellite	scene specification	geographic reference
SPOT	stereopair K=675, J=389	central Bolivia, Cerro Potosí mine
SPOT	stereopair K=673, J=387	central Bolivia, Uncia mine
SPOT	stereopair K=680, J=398	Jujuy, Arg., local seismic network
SPOT	stereopair K=675, J=413	C San Juan, Precordillera
SPOT	stereopair K=676, J=413	EC San Juan, Sierra Pie de Palo

Other

We have investigated two other types of imagery from central Asia, both from the Landsat satellites. Landsat Multispectral Scanner (MSS) images have approximately 80 m resolution and four spectral bands in the visible and near IR, while Landsat Thematic Mapper (TM) images have 30 m resolution and seven spectral bands in the visible, near IR, mid IR, and thermal IR. An MSS image was analyzed for an area of the Tadjik SSR that includes the areas covered by our SPOT stereopairs. The extra spectral information of MSS images does not make up for the relatively low resolution of the data. In fact, the MSS data was not very useful for interpreting geologic structures, fault scarps, or the locations of active mining because the 80 m resolution is not sufficient to resolve most of the features. The main advantage of MSS data is that the scenes are now

available at fairly low cost, only \$200 per 180 x 180 km scene for data that are more than two years old.

We received the Landsat Thematic Mapper scene for the Kazakhstan test sites (path 150, row 25 in the Landsat 4&5 Worldwide Reference System), and we have processed the data into IIS System 600 format to allow roaming and analysis on the IIS image displays. We have mapped the coordinates of the corners of the four quadrants (quads) of the scene and put those into ARC/INFO. ARC/INFO allows us to plot locations of published Soviet test locations (Vergino, 1989) with ISC seismic event locations and the TM quad locations and boundaries of the DTED cells (see Fig. 9). Roaming of the Shagan River test site in our standard TM 542 color composite (TM band 5 in red, band 4 in green, and band 2 in blue) lead to the discovery of some strange patches where the reflectance of the surface is low in the visible and high in the infrared, appearing orange in the 542 color scheme. Several of the patches seemed to be roughly circular in shape, but they appeared to be too far away from the obvious drill pads to be the surface expression of the underground nuclear tests. The cause of the unusual character of these patches remains unknown, but perhaps they could be related to old above-ground tests or some natural phenomenon.

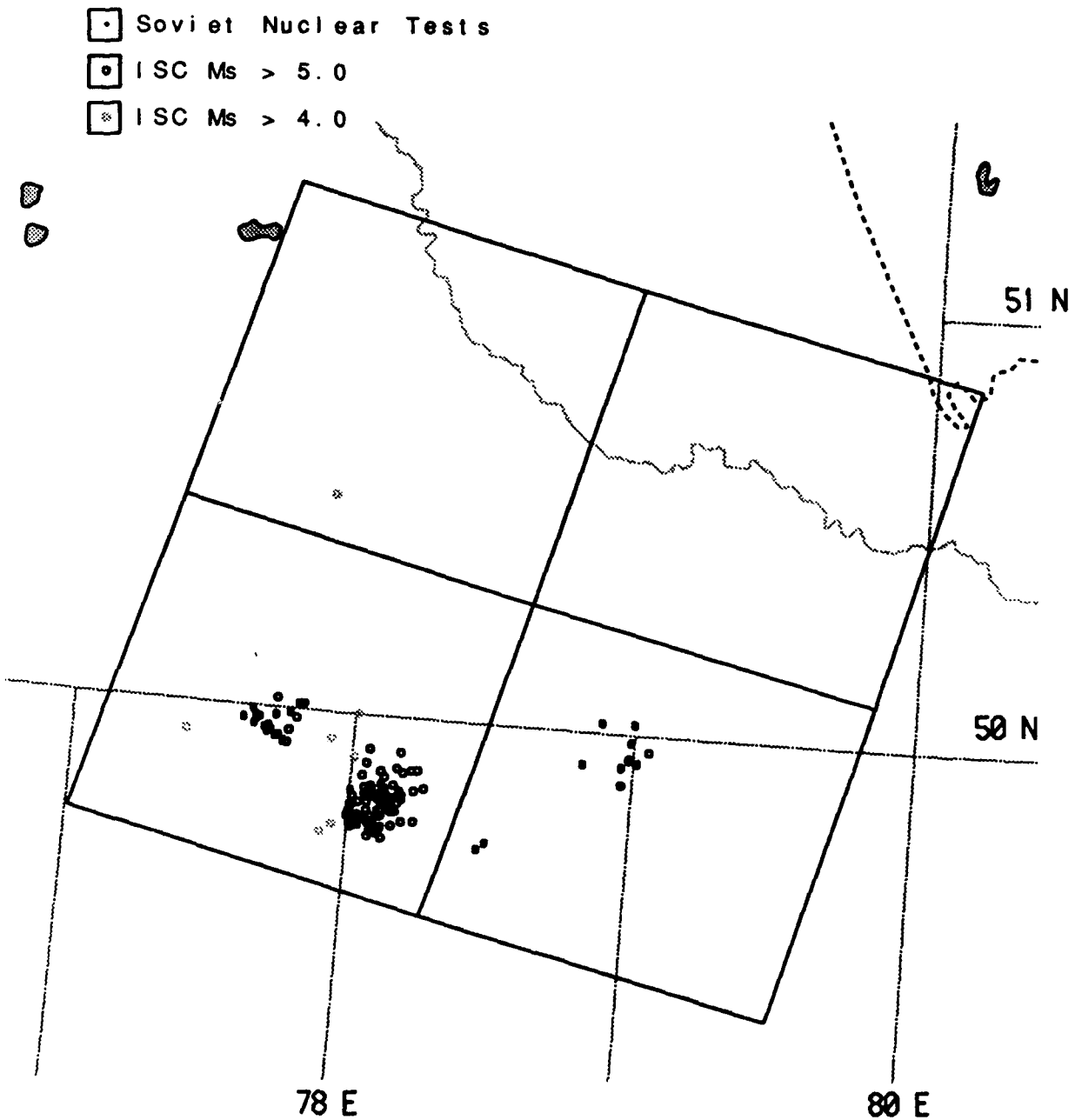


Figure 20. Map of the area around the Kazakhstan test site in the Soviet Union, showing seismic events, known explosions, and coverage of Landsat TM image, produced with ARC/INFO. Large parallelograms, *thin black lines*, show the boundaries of the four quadrants of the Landsat TM scene acquired for this area (WRS path 150, row 25). Boundaries of the DTED cells received are shown in *thin gray lines*. The Irtysh River is shown as a *medium gray line*, lakes are *filled gray with black borders*, and the Kazakh S.S.R.-Russian S.F.S.R. border is the *dashed line* in the NE corner of the map. As shown in the key, published locations of 93 Soviet nuclear tests (Vergino, 1989) are shown as *small filled squares* and ISC shallow ($z <$

50 km) event locations (1963–1984) with magnitudes (M_S) greater than 4.0 shown as *gray circles*, and events with M_S greater than 5.0 as *black circles*. Seismic event in the NW quadrant of the TM scene was a $m_b=5.1$ earthquake in 1976. See text for description of the TM features near this event.

We have used our experience with TM interpretation of late Cenozoic faults in the Andes (*e.g.*, Fielding and others, 1988; Fielding, 1989) to examine the TM data for the area in Kazakhstan near the location of the magnitude (m_b) 5.1 earthquake in 1976 about 100 km to the north of the nuclear test sites (see Figure 18). There is not a clear active fault scarp at the epicenter of the earthquake, but there is a more subtle, eroded scarp that runs for 10's of km through the area. This feature could be due to a buried fault or a fault that has not had enough displacement during the Quaternary to produce a scarp faster than the rate of erosion. The Quaternary erosion rate in Kazakhstan is likely to be greater than that of the Altiplano-Puna mapped previously because it now receives greater precipitation and presumably has been wetter throughout the Quaternary.

Comparisons

We performed a more detailed study of the Peter the First Range (PFR) near Garm, Soviet Tadjikistan, using our two SPOT stereopairs (see Figures 3 and 4) and other information. The area covered includes the new IRIS/IDA digital seismic station (GAR) now operating. A large catalog of locally recorded earthquakes for the PFR is being studied by Prof. Michael Hamburger and his colleagues at Indiana University in an ongoing project in collaboration with Soviet researchers to study the seismicity and structure in the Garm area (*e.g.*, Hamburger and others, 1988; Pavlis and others, 1988; Hamburger, *in review*). Our SPOT and topography data were compared with a Landsat MSS scene to look for evidence of surface faulting and also for evidence of mining operations

that could be the source of chemical explosions. This area has a very high level of seismicity, and is the site of several geologic and seismological studies (Burman and Gurariy, 1973; Trifonov, 1978; Burtman, 1980; Leith, 1982; Leith and Alvarez, 1985; Leith and Simpson, 1986).

We coregistered some of our DTED from the Garm, Tadjikistan area with a Landsat MSS (Multispectral Scanner) image. The moderate resolution (80 m) of the MSS data is close to that of the DTED, making the coregistration process straightforward. Control points (points such as stream intersections that are visible on both images) were selected and the DTED was resampled to fit the MSS scene. The generation of color 3D perspective images combines the topographic and satellite data into a new view of the earth's surface that shows more than either data set alone. The types of folds and faults can be determined more accurately because the dips of strata and fault surfaces and the slopes of fault scarps can be seen on the 3D imagery and the spectral bands of the MSS data provide information on the lithologies of the rocks. For instance, limestones show up as a bright blue color in the standard 421 MSS composites (unfortunately we cannot include color figures here). The SPOT stereopair for the area with its 10 m resolution (although only one wide spectral band) provides much more detailed structural information, albeit at much greater cost for the data.

We successfully adapted our existing digital mapping system to SPOT images, which are the primary satellite image source we will be using under this DARPA grant. A SPOT panchromatic image (one band, 10 m resolution) that we received under our NASA grant overlaps with part of the area mapped on the TM images (7 bands, 30 m resolution) and also an area studied in the field by one of our colleagues at Cornell. We used this as a test of the amount of information that could be extracted from the two types of imagery. The higher resolution

SPOT image showed some of the smaller (less offset and/or shorter length) faults that could not be seen on the TM images. The larger faults, with scarps of about 20 m or more as seen in the field, were visible on both types of imagery. A direct comparison of the fault locations mapped with our mapping system from the SPOT and TM images, using the geographic information provided with the imagery, showed a systematic difference in the absolute locations between the two images on the order of a few hundred meters.

We found that there was a systematic difference in the fault locations determined from TM images and those determined from SPOT images, in an area of the central Andes where our colleagues are doing field studies. To further study this locational discrepancy between the SPOT and TM image geographic information, we did an examination of one of the stereo pairs (each stereo pair acquired such that the SPOT satellite was looking at the same area on the ground from the east and the west) of SPOT panchromatic imagery from the San Juan province in Argentina. These images overlap with Landsat Thematic Mapper (TM) images that we had previously studied under our NASA grants, and provide a good basis for comparisons between the SPOT and TM imagery. The area also overlaps with an area under detailed study by seismologists at Cornell and Memphis State University with a 40 station digital seismograph array. The array was operated from September 1987 to April 1988, and recorded about 20,000 earthquakes of which nearly 3/4 were in the crust and the rest in the underlying Wadati-Benioff zone. Since the seismometer station locations were very precisely determined by a GPS (Global Positioning System) receiver (estimated error of about 10 m), we have determined the locations of several stations on the satellite imagery to compare the GPS locations with those determined purely from the geographic information provided in the imagery header

files. The results of this comparison for one of the SPOT images is shown in Table 6. It can be seen that the SPOT locations at the elevations around 600 m measured are within 330 m of their true positions.

Table 6. Comparison of Locations Determined from SPOT and GPS

Stn	elev.	GPS lat.	GPS lng	SPOT lat	SPOT lng	Δ lat	Δ long	total 'dist'
cf01	625m	-31.6028°	-68.2333°	-31.5987°	-68.2343°	-0.00418°	0.001039°	0.004305°
cf03	667m	-31.6054°	-68.2341°	-31.604°	-68.2335°	-0.00146°	-0.00054°	0.001557°
cf04	625m	-31.6029°	-68.2315°	-31.6001°	-68.2352°	-0.00282°	0.003725°	0.004673°
cf05	645m	-31.6049°	-68.2328°	-31.6035°	-68.2323°	-0.00134°	-0.00056°	0.00145°
cf07	615m	-31.6038°	-68.2319°	-31.6007°	-68.2335°	-0.00307°	0.001609°	0.003462°
cf10	655m	-31.6047°	-68.2298°	-31.6008°	-68.2314°	-0.00392°	0.001675°	0.004262°
Averages						-0.0028°	0.001158°	0.003285°
Converted to km						-0.31	0.10	0.33

A comparison was also done between the two SPOT scenes of one stereo pair and the corresponding TM image for features that could be identified as the same location on the images. The difference between the locations of three road intersections clearly visible on the two SPOT scenes was about 0.7 km in the same direction for each case. A different feature that was also clearly visible on the TM image was used for another comparison. The location determined from the TM image was about 0.8 km away from the locations determined from each of the two SPOT scenes. These discrepancies are unlikely to be due to inaccuracies in the equations we use to convert pixel coordinates to latitude and longitude, since we observed smaller discrepancies between overlapping TM images, or to inaccurate geographic information provided with the imagery, possibly due to topographic relief displacement.

DATA PRODUCTS

Products Generated

We produced moderate-resolution mosaics, at 1/10, 1/20, and 1/50 of the full resolution data for Central Asia, by mosaicking the mean elevations calculated from the 5° x 5° degree blocks with overlapping 20 x 20, 40 x 40, and 100 x 100 pixel windows applied to the full resolution data. The mean-value mosaics were projected into a Lambert Conformal Conic map projection at ~1, ~2, and ~5 km resolutions. A portion of the 1/10 resolution mosaic is shown in Figure 3. The 1/10 (~1 km resolution) mosaic is a moderate-size file (approximately 60 MB for the unprojected 16 bit data) that allows the whole data set to be examined at an interpretable resolution. We also produced 1/10 resolution mosaics for the Novaya Zemlya and Morocco datasets. We believe that these reduced-resolution topographic datasets should be very useful to DARPA researchers who model the effects of surface topography on the propagation of regional seismic phases.

We have produced digital versions of a variety of geological, geophysical and climatic maps, all stored in ARC/INFO a widely used Geographic Information System. These datasets include attributes associated with the digitized contours, faults and geologic units, and they have each been edited for consistency. We have produced a dataset of faults for Central Asia compiled from a large number of individual maps. This dataset includes attributes for the interpreted age and sense of motion for each fault, and an ID number that identifies the map source. All of the digitized datasets have been transformed from their original map projections into geographic coordinates of latitude and longitude.

Our Geological and Geophysical Information System (GGIS) has matured into an effective methodology. We have made our programs portable to other computer systems by coding them in the C language and using graphics subroutines that run on nearly all workstations and can use the Motif windowing system that is becoming a widely accepted standard (HOOPS, a three-dimensional graphics package from Ithaca Software). Our 3D perspective viewing program has proven to be portable to CSS machines, so we will improve the user interface and transfer a finished product to CSS. Other elements of our GGIS are built upon the IIS System 600 which is already in use at CSS and SAIC; and the Arc/Info package that also runs on both VAX and Sun workstations.

Plans to Transfer Products to CSS

We have continued our discussions with several of CSS personnel on how to best make our topography images and mosaics available on CSS systems. One relatively straightforward option is to create IIS System 600 image files that can be displayed on the IIS IVAS at the CSS. We were able to convert one of the images that we brought with us during a previous visit to CSS to IIS format and view it on the CSS IVAS. Another option is to create images that could be incorporated directly into the "Map" module of the Intelligent Monitoring System (IMS) running at the CSS. The latter option is more difficult but could be more useful in the long run for other CSS researchers. Unfortunately, at this time the "Map" is undergoing a major rewrite and details on the replacement module are not yet available as of this writing.

The transfer of the vector datasets from digitized maps is another subject of discussion. A simple file format that just contains the geographic coordinates of the points in the lines would lack the associated attributes of the various lines

such as the ages of the faults and lack the topological information of the polygon databases and their associated attributes. We will document all of our C code, Arc/Info macro programs, and processed datasets for DARPA use. We have not heard of any plans for the IMS to include an advanced GIS, but we would be glad to make our digital map datasets available, with their associated attributes and topological information, to be included into future version of the IMS that may have a use for such data.

CONCLUSIONS AND RECOMMENDATIONS

The integration of available vector datasets, such as digitized geologic and geophysical maps, with the virtual roam, rendering, and stereopair roam of the raster topography and images is leading to improved visualization of and insight into morphotectonic features that can bear on nuclear test discrimination and the propagation paths of crustal and lithospheric seismic phases. Geomorphic analysis, including evaluation of climatic effects, of the amount and age of activity is necessary to fully interpret fault scarps manifested in the topography. The zones of high precipitation are areas where we would predict that fault scarps and other geomorphic features associated with faults will be eroded and erased much more quickly than in drier areas. Conversely, in the extensive dry areas of Central Asia, we expect that manifestations of faulting should be clearly visible if deformation has occurred in geologically recent times. Inspection of available L_g propagation paths indicates a strong correlation between paths that lack observed high-frequency L_g to major topographic roughness. Future work to compare the wavelength spectra of topography along a path to the frequency spectra of L_g recordings should help quantify the magnitude of the effect.

REFERENCES

- Burtman, V.S., 1980, Faults of Middle Asia, *Am. J. Sci.*, v. 280, p. 725-744.
- Burtman, V.S., and G.Z. Gurariy, 1973, Character of folded arcs in the Pamirs and Tien Shan (from the geophysical data), *Geotectonics*, v. 3, p. 90-92.
- Chinn, D.S., B.L. Isacks, and M. Barazangi, 1980, High-frequency seismic wave propagation in western South America along the continental margin, in the Nazca plate and across the Altiplano, *Geophys. J. R. astr. Soc.*, v. 60, p. 209-244.
- D.M.A., 1986, Defense Mapping Agency product specifications for Digital Terrain Elevation Data (DTED), *DMA Aerospace Center, DTED 2nd Ed., PS/ICD/200*, 32 pp.
- Fielding, E.J., 1989, Neotectonics of the Central Andean Cordillera from satellite imagery, *Ph.D. dissertation, Cornell University*, 213 p.
- Fielding, E.J., Isacks, B.L., Allmendinger, R.W., and Marrett, R., 1988, Distribution of youthful faults and volcanic flows on the Altiplano-Puna plateau (abs.), *EOS*, v. 69, no. 44, p. 1439.
- Hamburger, M.W., W. Swanson, and I.L. Neresov, 1988, Seismicity and crustal structure within an active collisional orogen: Results from seismic networks in the Garm region, Soviet Central Asia, *EOS, Trans. AGU*, v. 69, no. 44, p. 1316.
- Hamburger, M.W., D.R. Sarewitz, and G.A. Popandopulo, in review, Structural and seismic evidence for intracontinental subduction in the Peter the First Range, Soviet Central Asia, submitted to *G. S. A. Bulletin*.
- Isacks, B.L., Uplift of the central Andean plateau and bending of the Bolivian orocline, *J. Geophys. Res.*, v. 93, p. 3211-3231.
- Kadinsky-Cade, K., M. Barazangi, J. Oliver, and B. Isacks, 1981, Lateral variations of high-frequency seismic wave propagation at regional distances across the Turkish and Iranian Plateaus, *J. Geophys. Res.*, v. 86, no. B10, p. 9377-9396.
- Kidd, W.S.F., ed., 1988, Geological map of the Academia Sinica-Royal Society Geotraverse route across the Xizang-Qinghai (Tibetan) plateau, 1:500,000 scale, *Phil. Trans. R. Soc. Lond., A*, v. 327, (map pocket).

- Kidd, W.S.F., Pan Y., Chang C., M.P. Coward, J.F. Dewey, A. Gansser, P. Molnar, R.M. Shackleton, and Sun Y., 1988, Geological mapping of the 1985 Chinese-British Tibetan (Xizang-Qinghai) Plateau Geotraverse route, *Phil. Trans. R. Soc. Lond., A*, v. 327, p. 287-305.
- Leith, W., 1982, Rock assemblages in Central Asia and the evolution of the southern Asian margin, *Tectonics*, v. 1, p. 303-318.
- Leith, W., and D.W. Simpson, 1986, Seismic domains within the Gissar-Kokshal seismic zone, Soviet Central Asia, *J. Geophys. Res.*, v. 91, p. 689-697.
- Leith, W., and W. Alvarez, 1985, Structure of the Vakhsh fold and thrust belt, Tadjik SSR: An application of Landsat imagery to continuous-structure mapping, *Geol. Soc. Amer. Bull.*, v. 96, p. 875-885.
- Ni, J., and M. Barazangi, 1983, High-frequency seismic wave propagation beneath the Indian Shield, Himalayan Arc, Tibetan Plateau and surrounding regions: high uppermost mantle velocities and efficient S_n propagation beneath Tibet, *Geophys. J. R. astr. Soc.*, v. 72, p. 665-689.
- Pavlis, G.L., M. Eneva, M.W. Hamburger, and I.L. Neresov, 1988, Aftershock properties in the Garm region, USSR, *EOS, Trans. AGU*, v. 69, no. 44, p. 1316.
- Ruzaikan, A.I., I.L. Neresov, V.I. Khalturin, and P. Molnar, 1977, Propagation of L_g and lateral variation in crustal structure in Asia, *J. Geophys. Res.*, v. 82, p. 307-316.
- Trifonov, V.G., 1978, Late Quaternary tectonic movements of western and central Asia, *Geol. Soc. Amer. Bull.*, v. 89, p. 1059-1072.
- Trifonov, V.G., ed., 1986, Map of active faults of the USSR and the adjacent areas, 1:8,000,000 scale, Moscow-Irkutsk.
- U.S.G.S., 1986, Standards for digital elevation models, *U.S. Geol. Surv. National Mapping Division, Open-File Report 86-004*, 41 pp.
- U.S.G.S., 1987, Digital elevation models, *U.S. Geol. Surv. National Mapping Program, Technical Instructions, Data Users Guide 5*, 38 pp.
- Vergino, E.S., 1989, Soviet Test Yields, *EOS*, v.70, no. 48, p. 1511&1524-1525.

Prof. Thomas Ahrens
Seismological Lab, 252-21
Division of Geological & Planetary Sciences
California Institute of Technology
Pasadena, CA 91125

Prof. Charles B. Archambeau
CIRES
University of Colorado
Boulder, CO 80309

Dr. Thomas C. Bache, Jr.
Science Applications Int'l Corp.
10260 Campus Point Drive
San Diego, CA 92121 (2 copies)

Prof. Muawia Barazangi
Institute for the Study of the Continent
Cornell University
Ithaca, NY 14853

Dr. Jeff Barker
Department of Geological Sciences
State University of New York
at Binghamton
Vestal, NY 13901

Dr. Douglas R. Baumgardt
ENSCO, Inc
5400 Port Royal Road
Springfield, VA 22151-2388

Prof. Jonathan Berger
IGPP, A-025
Scripps Institution of Oceanography
University of California, San Diego
La Jolla, CA 92093

Dr. Gilbert A. Bollinger
Department of Geological Sciences
Virginia Polytechnical Institute
21044 Derring Hall
Blacksburg, VA 24061

Dr. Lawrence J. Burdick
Woodward-Clyde Consultants
566 El Dorado Street
Pasadena, CA 91109-3245

Dr. Jerry Carter
Center for Seismic Studies
1300 North 17th St., Suite 1450
Arlington, VA 22209-2308

Dr. Karl Coyner
New England Research, Inc.
76 Olcott Drive
White River Junction, VT 05001

Prof. Vernon F. Cormier
Department of Geology & Geophysics
U-45, Room 207
The University of Connecticut
Storrs, CT 06268

Professor Anton W. Dainty
Earth Resources Laboratory
Massachusetts Institute of Technology
42 Carleton Street
Cambridge, MA 02142

Prof. Steven Day
Department of Geological Sciences
San Diego State University
San Diego, CA 92182

Dr. Zoltan A. Der
ENSCO, Inc.
5400 Port Royal Road
Springfield, VA 22151-2388

Prof. Lewis M. Duncan
Dept. of Physics & Astronautics
Clemson University
Clemson, SC 29634-1901

Prof. John Ferguson
Center for Lithospheric Studies
The University of Texas at Dallas
P.O. Box 830688
Richardson, TX 75083-0688

Dr. Mark D. Fisk
Mission Research Corporation
735 State Street
P. O. Drawer 719
Santa Barbara, CA 93102

Prof. Stanley Flatte
Applied Sciences Building
University of California
Santa Cruz, CA 95064

Dr. Alexander Florence
SRI International
333 Ravenswood Avenue
Menlo Park, CA 94025-3493

Dr. Holy K. Given
IGPP, A-025
Scripps Institute of Oceanography
University of California, San Diego
La Jolla, CA 92093

Prof. Henry L. Gray
Vice Provost and Dean
Department of Statistical Sciences
Southern Methodist University
Dallas, TX 75275

Dr. Indra Gupta
Teledyne Geotech
314 Montgomery Street
Alexandria, VA 22314

Prof. David G. Harkrider
Seismological Laboratory
Division of Geological & Planetary Sciences
California Institute of Technology
Pasadena, CA 91125

Prof. Danny Harvey
CIRES
University of Colorado
Boulder, CO 80309

Prof. Donald V. Helmberger
Seismological Laboratory
Division of Geological & Planetary Sciences
California Institute of Technology
Pasadena, CA 91125

Prof. Eugene Herrin
Institute for the Study of Earth and Man
Geophysical Laboratory
Southern Methodist University
Dallas, TX 75275

Prof. Bryan Isacks
Cornell University
Department of Geological Sciences
SNEE Hall
Ithaca, NY 14850

Dr. Rong-Song Jih
Teledyne Geotech
314 Montgomery Street
Alexandria, VA 22314

Prof. Lane R. Johnson
Seismographic Station
University of California
Berkeley, CA 94720

Dr. Richard LaCoss
MIT-Lincoln Laboratory
M-200B
P. O. Box 73
Lexington, MA 02173-0073 (3 copies)

Prof Fred K. Lamb
University of Illinois at Urbana-Champaign
Department of Physics
1110 West Green Street
Urbana, IL 61801

Prof. Charles A. Langston
Geosciences Department
403 Deike Building
The Pennsylvania State University
University Park, PA 16802

Prof. Thorne Lay
Institute of Tectonics
Earth Science Board
University of California, Santa Cruz
Santa Cruz, CA 95064

Prof. Arthur Lerner-Lam
Lamont-Doherty Geological Observatory
of Columbia University
Palisades, NY 10964

Dr. Christopher Lynnes
Teledyne Geotech
314 Montgomery Street
Alexandria, VA 22314

Prof. Peter Malin
Department of Geology
Old Chemistry Bldg.
Duke University
Durham, NC 27706

Dr. Randolph Martin, III
New England Research, Inc.
76 Olcott Drive
White River Junction, VT 05001

Prof. Thomas V. McEvilly
Seismographic Station
University of California
Berkeley, CA 94720

Dr. Keith L. McLaughlin
S-CUBED
A Division of Maxwell Laboratory
P.O. Box 1620
La Jolla, CA 92038-1620

Prof. William Menke
Lamont-Doherty Geological Observatory
of Columbia University
Palisades, NY 10964

Prof. Charles G. Sammis
Center for Earth Sciences
University of Southern California
University Park
Los Angeles, CA 90089-0741

Stephen Miller
SRI International
333 Ravenswood Avenue
Box AF 116
Menlo Park, CA 94025-3493

Prof. Christopher H. Scholz
Lamont-Doherty Geological Observatory
of Columbia University
Palisades, NY 10964

Prof. Bernard Minster
IGPP, A-025
Scripps Institute of Oceanography
University of California, San Diego
La Jolla, CA 92093

Thomas J. Sereno, Jr.
Science Application Int'l Corp.
10260 Campus Point Drive
San Diego, CA 92121

Prof. Brian J. Mitchell
Department of Earth & Atmospheric Sciences
St. Louis University
St. Louis, MO 63156

Prof. David G. Simpson
Lamont-Doherty Geological Observatory
of Columbia University
Palisades, NY 10964

Mr. Jack Murphy
S-CUBED, A Division of Maxwell Laboratory
11800 Sunrise Valley Drive
Suite 1212
Reston, VA 22091 (2 copies)

Dr. Jeffrey Stevens
S-CUBED
A Division of Maxwell Laboratory
P.O. Box 1620
La Jolla, CA 92038-1620

Prof. John A. Orcutt
IGPP, A-025
Scripps Institute of Oceanography
University of California, San Diego
La Jolla, CA 92093

Prof. Brian Stump
Institute for the Study of Earth & Man
Geophysical Laboratory
Southern Methodist University
Dallas, TX 75275

Prof. Keith Priestley
University of Cambridge
Bullard Labs, Dept. of Earth Sciences
Madingley Rise, Madingley Rd.
Cambridge CB3 0EZ, ENGLAND

Prof. Jeremiah Sullivan
University of Illinois at Urbana-Champaign
Department of Physics
1110 West Green Street
Urbana, IL 61801

Dr. Jay J. Pulli
Radix Systems, Inc.
2 Taft Court, Suite 203
Rockville, MD 20850

Prof. Clifford Thurber
University of Wisconsin-Madison
Department of Geology & Geophysics
1215 West Dayton Street
Madison, WI 53706

Prof. Paul G. Richards
Lamont Doherty Geological Observatory
of Columbia University
Palisades, NY 10964

Prof. M. Nafi Toksoz
Earth Resources Lab
Massachusetts Institute of Technology
42 Carleton Street
Cambridge, MA 02142

Dr. Wilmer Rivers
Teledyne Geotech
314 Montgomery Street
Alexandria, VA 22314

Prof. John E. Vidale
University of California at Santa Cruz
Seismological Laboratory
Santa Cruz, CA 95064

Prof. Terry C. Wallace
Department of Geosciences
Building #77
University of Arizona
Tucson, AZ 85721

Dr. William Wortman
Mission Research Corporation
8560 Cinderbed Rd.
Suite # 700
Newington, VA 22122

Prof. Francis T. Wu
Department of Geological Sciences
State University of New York
at Binghamton
Vestal, NY 13901

OTHERS (United States)

Dr. Monem Abdel-Gawad
Rockwell International Science Center
1049 Camino Dos Rios
Thousand Oaks, CA 91360

Michael Browne
Teledyne Geotech
3401 Shiloh Road
Garland, TX 75041

Prof. Keiiti Aki
Center for Earth Sciences
University of Southern California
University Park
Los Angeles, CA 90089-0741

Mr. Roy Burger
1221 Serry Road
Schenectady, NY 12309

Prof. Shelton S. Alexander
Geosciences Department
403 Deike Building
The Pennsylvania State University
University Park, PA 16802

Dr. Robert Burrige
Schlumberger-Doll Research Center
Old Quarry Road
Ridgefield, CT 06877

Dr. Kenneth Anderson
BBNSTC
Mail Stop 14/1B
Cambridge, MA 02238

Dr. W. Winston Chan
Teledyne Geotech
314 Montgomery Street
Alexandria, VA 22314-1581

Dr. Ralph Archuleta
Department of Geological Sciences
University of California at Santa Barbara
Santa Barbara, CA 93102

Dr. Theodore Cherry
Science Horizons, Inc.
710 Encinitas Blvd., Suite 200
Encinitas, CA 92024 (2 copies)

Dr. Susan Beck
Department of Geosciences
Bldg. # 77
University of Arizona
Tucson, AZ 85721

Prof. Jon F. Clacrbout
Department of Geophysics
Stanford University
Stanford, CA 94305

Dr. T.J. Bennett
S-CUBED
A Division of Maxwell Laboratory
11800 Sunrise Valley Drive, Suite 1212
Reston, VA 22091

Prof. Robert W. Clayton
Seismological Laboratory
Division of Geological & Planetary Sciences
California Institute of Technology
Pasadena, CA 91125

Mr. William J. Best
907 Westwood Drive
Vienna, VA 22180

Prof. F. A. Dahlen
Geological and Geophysical Sciences
Princeton University
Princeton, NJ 08544-0636

Dr. N. Biswas
Geophysical Institute
University of Alaska
Fairbanks, AK 99701

Mr. Charles Doll
Earth Resources Laboratory
Massachusetts Institute of Technology
42 Carleton St.
Cambridge, MA 02142

Dr. Stephen Bratt
Center for Seismic Studies
1300 North 17th Street
Suite 1450
Arlington, VA 22209

Prof. Adam Dziewonski
Hoffman Laboratory, Harvard Univ.
Dept. of Earth Atmos. & Planetary Sciences
20 Oxford St
Cambridge, MA 02138

Prof. John Ebel
Department of Geology & Geophysics
Boston College
Chestnut Hill, MA 02167

Eric Fielding
SNEE Hall
INSTOC
Cornell University
Ithaca, NY 14853

Dr. John Foley
Phillips Laboratory/LWH
Hanscom AFB, MA 01731-5000

Prof. Donald Forsyth
Department of Geological Sciences
Brown University
Providence, RI 02912

Dr. Cliff Frolich
Institute of Geophysics
8701 North Mopac
Austin, TX 78759

Dr. Anthony Gangi
Texas A&M University
Department of Geophysics
College Station, TX 77843

Dr. Freeman Gilbert
IGPP, A-025
Scripps Institute of Oceanography
University of California
La Jolla, CA 92093

Mr. Edward Giller
Pacific Sierra Research Corp.
1401 Wilson Boulevard
Arlington, VA 22209

Dr. Jeffrey W. Given
SAIC
10260 Campus Point Drive
San Diego, CA 92121

Prof. Stephen Grand
University of Texas at Austin
Department of Geological Sciences
Austin, TX 78713-7909

Prof. Roy Greenfield
Geosciences Department
403 Deike Building
The Pennsylvania State University
University Park, PA 16802

Dan N. Hagedorn
Battelle
Pacific Northwest Laboratories
Battelle Boulevard
Richland, WA 99352

Dr. James Hannon
Lawrence Livermore National Laboratory
P. O. Box 808
Livermore, CA 94550

Prof. Robert B. Herrmann
Dept. of Earth & Atmospheric Sciences
St. Louis University
St. Louis, MO 63156

Ms. Heidi Houston
Seismological Laboratory
University of California
Santa Cruz, CA 95064

Kevin Hutchenson
Department of Earth Sciences
St. Louis University
3507 Laclede
St. Louis, MO 63103

Dr. Hans Israelsson
Center for Seismic Studies
1300 N. 17th Street, Suite 1450
Arlington, VA 22209-2308

Prof. Thomas H. Jordan
Department of Earth, Atmospheric
and Planetary Sciences
Massachusetts Institute of Technology
Cambridge, MA 02139

Prof. Alan Kafka
Department of Geology & Geophysics
Boston College
Chestnut Hill, MA 02167

Robert C. Kemerait
ENSCO, Inc.
445 Pineda Court
Melbourne, FL 32940

William Kikendall
Teledyne Geotech
3401 Shiloh Road
Garland, TX 75041

Prof. Leon Knopoff
University of California
Institute of Geophysics & Planetary Physics
Los Angeles, CA 90024

Prof. John Kuo
Aldridge Laboratory of Applied Geophysics
Columbia University
842 Mudd Bldg.
New York, NY 10027

Prof. L. Timothy Long
School of Geophysical Sciences
Georgia Institute of Technology
Atlanta, GA 30332

Dr. Gary McCartor
Department of Physics
Southern Methodist University
Dallas, TX 75275

Prof. Art McGarr
Mail Stop 977
Geological Survey
345 Middlefield Rd.
Menlo Park, CA 94025

Dr. George Mellman
Sierra Geophysics
11255 Kirkland Way
Kirkland, WA 98033

Prof. John Nabelek
College of Oceanography
Oregon State University
Corvallis, OR 97331

Prof. Geza Nagy
University of California, San Diego
Department of Ames, M.S. B-010
La Jolla, CA 92093

Dr. Keith K. Nakanishi
Lawrence Livermore National Laboratory
L-205
P. O. Box 808
Livermore, CA 94550

Prof. Amos Nur
Department of Geophysics
Stanford University
Stanford, CA 94305

Prof. Jack Oliver
Department of Geology
Cornell University
Ithaca, NY 14850

Dr. Kenneth Olsen
P. O. Box 1273
Linwood, WA 98046-1273

Prof. Jeffrey Park
Department of Geology and Geophysics
Kline Geology Laboratory
P. O. Box 6666
New Haven, CT 06511-8130

Howard J. Patton
Lawrence Livermore National Laboratory
L-205
P. O. Box 808
Livermore, CA 94550

Prof. Robert Phinney
Geological & Geophysical Sciences
Princeton University
Princeton, NJ 08544-0636

Dr. Paul Pomeroy
Rondout Associates
P.O. Box 224
Stone Ridge, NY 12484

Dr. Norton Rimer
S-CUBED
A Division of Maxwell Laboratory
P.O. Box 1620
La Jolla, CA 92038-1620

Prof. Larry J. Ruff
Department of Geological Sciences
1006 C.C. Little Building
University of Michigan
Ann Arbor, MI 48109-1063

Dr. Richard Sailor
TASC Inc.
55 Walkers Brook Drive
Reading, MA 01867

Dr. Susan Schwartz
Institute of Tectonics
1156 High St.
Santa Cruz, CA 95064

John Sherwin
Teledyne Geotech
3401 Shiloh Road
Garland, TX 75041

Dr. Matthew Sibol
Virginia Tech
Seismological Observatory
4044 Derring Hall
Blacksburg, VA 24061-0420

Dr. Albert Smith
Lawrence Livermore National Laboratory
L-205
P. O. Box 808
Livermore, CA 94550

Prof. Robert Smith
Department of Geophysics
University of Utah
1400 East 2nd South
Salt Lake City, UT 84112

Dr. Stewart W. Smith
Geophysics AK-50
University of Washington
Seattle, WA 98195

Donald L. Springer
Lawrence Livermore National Laboratory
L-205
P. O. Box 808
Livermore, CA 94550

Dr. George Sutton
Rondout Associates
P.O. Box 224
Stone Ridge, NY 12484

Prof. L. Sykes
Lamont-Doherty Geological Observatory
of Columbia University
Palisades, NY 10964

Prof. Pradeep Talwani
Department of Geological Sciences
University of South Carolina
Columbia, SC 29208

Dr. David Taylor
ENSCO, Inc.
445 Pineda Court
Melbourne, FL 32940

Dr. Steven R. Taylor
Lawrence Livermore National Laboratory
L-205
P. O. Box 808
Livermore, CA 94550

Professor Ta-Liang Teng
Center for Earth Sciences
University of Southern California
University Park
Los Angeles, CA 90089-0741

Dr. Gregory van der Vink
IRIS, Inc.
1616 North Fort Myer Drive
Suite 1440
Arlington, VA 22209

Professor Daniel Walker
University of Hawaii
Institute of Geophysics
Honolulu, HI 96822

William R. Walter
Seismological Laboratory
University of Nevada
Reno, NV 89557

Dr. Raymond Willeman
Phillips Laboratory - OL-AA/LWH
Hanscom AFB, MA 01731-5000

Dr. Gregory Wojcik
Weidlinger Associates
4410 El Camino Real
Suite 110
Los Altos, CA 94022

Dr. Lorraine Wolf
Phillips Laboratory/LWH
Hanscom AFB, MA 01731-5000

Dr. Gregory B. Young
ENSCO, Inc.
5400 Port Royal Road
Springfield, VA 22151-2388

Dr. Eileen Vergino
Lawrence Livermore National Laboratory
L-205
P. O. Box 808
Livermore, CA 94550

• J. J. Zucca
Lawrence Livermore National Laboratory
P. O. Box 808
• Livermore, CA 94550

GOVERNMENT

Dr. Ralph Alewine III
DARPA/NMRO
1400 Wilson Boulevard
Arlington, VA 22209-2308

Mr. James C. Battis
Phillips Laboratory/LWH
Hanscom AFB, MA 01731-5000

Harley Benz
U.S. Geological Survey, MS-977
345 Middlefield Rd.
Menlo Park, CA 94025

Dr. Robert Blandford
AFTAC/TT
Center for Seismic Studies
1300 North 17th St. Suite 1450
Arlington, VA 22209-2308

Eric Chael
Division 9241
Sandia Laboratory
Albuquerque, NM 87185

Dr. John J. Cipar
Phillips Laboratory/LWH
Hanscom AFB, MA 01731-5000

Cecil Davis
Group P-15, Mail Stop D406
P.O. Box 1663
Los Alamos National Laboratory
Los Alamos, NM 87544

Mr. Jeff Duncan
Office of Congressman Markey
2133 Rayburn House Bldg.
Washington, DC 20515

Dr. Jack Evernden
USGS - Earthquake Studies
345 Middlefield Road
Menlo Park, CA 94025

Art Frankel
USGS
922 National Center
Reston, VA 22092

Dr. Dale Glover
DIA/DT-1B
Washington, DC 20301

Dr. T. Hanks
USGS
Nat'l Earthquake Research Center
345 Middlefield Road
Menlo Park, CA 94025

Dr. Roger Hansen
AFTAC/TT
Patrick AFB, FL 32925

Paul Johnson
ESS-4, Mail Stop J979
Los Alamos National Laboratory
Los Alamos, NM 87545

Janet Johnston
Phillips Laboratory/LWH
Hanscom AFB, MA 01731-5000

Dr. Katharine Kadinsky-Cade
Phillips Laboratory/LWH
Hanscom AFB, MA 01731-5000

Ms. Ann Kerr
IGPP, A-025
Scripps Institute of Oceanography
University of California, San Diego
La Jolla, CA 92093

Dr. Max Koontz
US Dept of Energy/DP 5
Forrestal Building
1000 Independence Avenue
Washington, DC 20585

Dr. W.H.K. Lee
Office of Earthquakes, Volcanoes,
& Engineering
345 Middlefield Road
Menlo Park, CA 94025

Dr. William Leith
U.S. Geological Survey
Mail Stop 928
Reston, VA 22092

Dr. Richard Lewis
Director, Earthquake Engineering & Geophysics
U.S. Army Corps of Engineers
Box 631
Vicksburg, MS 39180

• James F. Lewkowicz
Phillips Laboratory/LWH
Hanscom AFB, MA 01731-5000

Mr. Alfred Lieberman
ACDA/VI-OA'State Department Bldg
Room 5726
320 - 21st Street, NW
Washington, DC 20451

Stephen Mangino
Phillips Laboratory/LWH
Hanscom AFB, MA 01731-5000

Dr. Robert Masse
Box 25046, Mail Stop 967
Denver Federal Center
Denver, CO 80225

Art McGarr
U.S. Geological Survey, MS-977
345 Middlefield Road
Menlo Park, CA 94025

Richard Morrow
ACDA/VI, Room 5741
320 21st Street N.W
Washington, DC 20451

Dr. Carl Newton
Los Alamos National Laboratory
P.O. Box 1663
Mail Stop C335, Group ESS-3
Los Alamos, NM 87545

• Dr. Bao Nguyen
AFTAC/TTR
Patrick AFB, FL 32925

Dr. Kenneth H. Olsen
Los Alamos Scientific Laboratory
P. O. Box 1663
Mail Stop D-406
Los Alamos, NM 87545

Mr. Chris Paine
Office of Senator Kennedy
SR 315
United States Senate
Washington, DC 20510

Colonel Jerry J. Perrizo
AFOSR/NP, Building 410
Bolling AFB
Washington, DC 20332-6448

Dr. Frank F. Pilotte
HQ AFTAC/TT
Patrick AFB, FL 32925-6001

Katie Poley
CIA-ACIS/TMC
Room 4X16NHB
Washington, DC 20505

Mr. Jack Rachlin
U.S. Geological Survey
Geology, Rm 3 C136
Mail Stop 928 National Center
Reston, VA 22092

Dr. Robert Reinke
WL/NTESG
Kirtland AFB, NM 87117-6008

Dr. Byron Ristvet
HQ DNA, Nevada Operations Office
Attn: NVCG
P.O. Box 98539
Las Vegas, NV 89193

Dr. George Rothe
HQ AFTAC/TTR
Patrick AFB, FL 32925-6001

Dr. Alan S. Ryall, Jr.
DARPA/NMRO
1400 Wilson Boulevard
Arlington, VA 22209-2308

Dr. Michael Shore
Defense Nuclear Agency/SPSS
6801 Telegraph Road
Alexandria, VA 22310

Mr. Charles L. Taylor
Phillips Laboratory/LWH
Hanscom AFB, MA 01731-5000

Phillips Laboratory
Attn: XO
Hanscom AFB, MA 01731-5000

Dr. Larry Turnbull
CIA-OSWR/NED
Washington, DC 20505

Phillips Laboratory
Attn: LW
Hanscom AFB, MA 01731-5000

Dr. Thomas Weaver
Los Alamos National Laboratory
P.O. Box 1663, Mail Stop C335
Los Alamos, NM 87545

DARPA/PM
1400 Wilson Boulevard
Arlington, VA 22209

Phillips Laboratory
Research Library
ATTN: SULL
Hanscom AFB, MA 01731-5000 (2 copies)

Defense Technical Information Center
Cameron Station
Alexandria, VA 22314 (5 copies)

Phillips Laboratory
ATTN: SUL
Kirtland AFB, NM 87117-6008

Defense Intelligence Agency
Directorate for Scientific & Technical Intelligence
Attn: DT1B
Washington, DC 20340-6158

Secretary of the Air Force
(SAFRD)
Washington, DC 20330

AFTAC/CA
(STINFO)
Patrick AFB, FL 32925-6001

Office of the Secretary Defense
DDR & E
Washington, DC 20330

TACTEC
Battelle Memorial Institute
505 King Avenue
Columbus, OH 43201 (Final Report Only)

HQ DNA
Attn: Technical Library
Washington, DC 20305

DARPA/RMO/RETRIEVAL
1400 Wilson Boulevard
Arlington, VA 22209

DARPA/RMO/Security Office
1400 Wilson Boulevard
Arlington, VA 22209

CONTRACTORS (FOREIGN)

Dr. Ramon Cabre, S.J.
Observatorio San Calixto
Casilla 5939
La Paz, Bolivia

Prof. Hans-Peter Harjes
Institute for Geophysik
Ruhr University/Bochum
P.O. Box 102148
4630 Bochum 1, FRG

Prof. Eystein Husebye
NTNF/NORSAR
P.O. Box 51
N-2007 Kjeller, NORWAY

Prof. Brian L.N. Kennett
Research School of Earth Sciences
Institute of Advanced Studies
G.P.O. Box 4
Canberra 2601, AUSTRALIA

Dr. Bernard Massinon
Societe Radiomana
27 rue Claude Bernard
75005 Paris, FRANCE (2 Copies)

Dr. Pierre Mecheler
Societe Radiomana
27 rue Claude Bernard
75005 Paris, FRANCE

Dr. Svein Mykkeltveit
NTNF/NORSAR
P.O. Box 51
N-2007 Kjeller, NORWAY (3 copies)

FOREIGN (OTHERS)

Dr. Peter Basham
Earth Physics Branch
Geological Survey of Canada
1 Observatory Crescent
Ottawa, Ontario, CANADA K1A 0Y3

Dr. Eduard Berg
Institute of Geophysics
University of Hawaii
Honolulu, HI 96822

Dr. Michel Bouchon
I.R.I.G.M.-B.P. 68
38402 St. Martin D'Herès
Cedex, FRANCE

Dr. Hilmar Bungum
NTNF/NORSAR
P.O. Box 51
N-2007 Kjeller, NORWAY

Dr. Michel Campillo
Observatoire de Grenoble
I.R.I.G.M.-B.P. 53
38041 Grenoble, FRANCE

Dr. Kin Yip Chun
Geophysics Division
Physics Department
University of Toronto
Ontario, CANADA M5S 1A7

Dr. Alan Douglas
Ministry of Defense
Blacknest, Brimpton
Reading RG7-4RS, UNITED KINGDOM

Dr. Manfred Henger
Federal Institute for Geosciences & Nat'l Res.
Postfach 510153
D-3000 Hanover 51, FRG

Ms. Eva Johannisson
Senior Research Officer
National Defense Research Inst.
P.O. Box 27322
S-102 54 Stockholm, SWEDEN

Dr. Fekadu Kebede
Geophysical Observatory, Science Faculty
Addis Ababa University
P. O. Box 1176
Addis Ababa, ETHIOPIA

Dr. Tormod Kvaerna
NTNF/NORSAR
P.O. Box 51
N-2007 Kjeller, NORWAY

Dr. Peter Marshall
Procurement Executive
Ministry of Defense
Blacknest, Brimpton
Reading FG7-4RS, UNITED KINGDOM

Prof. Ari Ben-Menahem
Department of Applied Mathematics
Weizman Institute of Science
Rehovot, ISRAEL 951729

Dr. Robert North
Geophysics Division
Geological Survey of Canada
1 Observatory Crescent
Ottawa, Ontario, CANADA K1A 0Y3

Dr. Frode Ringdal
NTNF/NORSAR
P.O. Box 51
N-2007 Kjeller, NORWAY

Dr. Jorg Schlittenhardt
Federal Institute for Geosciences & Nat'l Res.
Postfach 510153
D-3000 Hannover 51, FEDERAL REPUBLIC OF
GERMANY

Universita Degli Studi Di Trieste
Facolta Di Ingegneria
Istituto Di Miniere E. Geofisica Applicata, Trieste,
ITALY

Dr. John Woodhouse
Oxford University
Dept of Earth Sciences
Parks Road
Oxford OX13PR, ENGLAND